

RXJ0142.0+2131: I. THE GALAXY CONTENT OF AN X-RAY-LUMINOUS GALAXY CLUSTER AT $z = 0.28$

JORDI BARR, ROGER DAVIES
 Oxford University, Keble Road, Oxford, OX1 3RH, UK

INGER JØRGENSEN
 Gemini Observatory, Hilo, Hawaii, USA

MARCEL BERGMANN
 NOAO Gemini Science Center, La Serena, Chile

AND

DAVID CRAMPTON
 Herzberg Institute of Astrophysics, Canada
Draft version April 14, 2017

ABSTRACT

We present a photometric and spectroscopic study of stellar populations in the X-ray-luminous cluster of galaxies RXJ0142.0+2131 at $z = 0.280$. This paper analyses the results of high signal-to-noise spectroscopy, as well as g' -, r' -, and i' -band imaging, using the Gemini Multi-Object Spectrograph on Gemini North. Of 43 spectroscopic targets, we find 30 cluster members over a range in color. Central velocity dispersions and absorption-line strengths for lines in the range $3700\text{\AA} \lesssim \lambda_{\text{rest}} \lesssim 5800\text{\AA}$ are derived for cluster members, and are compared with a low-redshift sample of cluster galaxies, and single stellar population (SSP) models. We use a combination of these indicators to estimate luminosity-weighted mean ages, metallicities ($[M/H]$), and α -element abundance ratios ($[\alpha/Fe]$).

RXJ0142.0+2131 is a relatively poor cluster and lacks galaxies with high central velocity dispersions. Although the red sequence and the Faber-Jackson relation are consistent with pure passive evolution of the early-type population with a formation redshift of $z_{\text{form}} \simeq 2$, the strengths of the 4000\AA break and scaling relations between metal line indices and velocity dispersion reject this model with high significance. By inverting SSP models for the $H\beta_G$, Mgb , and $\langle Fe \rangle$ line indices, we calculate that, at a given velocity dispersion and metallicity, galaxies in RXJ0142.0+2131 have luminosity-weighted mean ages 0.14 ± 0.07 dex older than the low-redshift sample. We also find that $[\alpha/Fe]$ in stellar populations in RXJ0142.0+2131 is 0.14 ± 0.03 greater than at low redshift. All scaling relations are consistent with these estimated offsets.

We speculate that the older luminosity-weighted mean ages and $[\alpha/Fe]$ enhancement can be brought about by a rapidly-curtailed burst of star formation in RXJ0142.0+2131, such as may be experienced in a cluster-cluster merger. We note that the cluster's velocity dispersion, $1278 \pm 134 \text{ km s}^{-1}$, is larger than expected both from its X-ray luminosity and richness. However, the velocity distribution of galaxies in RXJ0142.0+2131 is consistent with being drawn from a Gaussian distribution and no sign of substructure is found. We conclude that stellar populations in RXJ0142.0+2131 cannot evolve into stellar populations similar to those seen in our low-redshift sample through passive evolution. This study provides further evidence that a more complex model, possibly involving ongoing or intermittent star formation and galaxy mergers, is required to describe the evolution of cluster galaxies.

Subject headings: galaxies: clusters: individual: RXJ0142.0+2131 – galaxies: evolution – galaxies: stellar content

1. INTRODUCTION

Studies of the kinematic properties of galaxies in local clusters have revealed a number of empirical scaling relations. Primary among these is the Fundamental Plane (FP) of elliptical (E) and lenticular (S0) galaxies, (e.g. Djorgovski & Davis 1987; Dressler et al. 1987; Jørgensen et al. 1996), which relates surface brightness, effective ra-

dius and central velocity dispersion in cluster members. This can be projected to give a correlation between luminosity and velocity dispersion, the Faber-Jackson (FJ) relation (Faber & Jackson 1976). For spiral galaxies, the Tully-Fisher (TF) relation (Aaronson et al. 1986) gives the relationship between luminosity and rotational velocity. Also well-studied is the red sequence of early-type galaxies (e.g. Bower et al. 1992; Kodama & Arimoto 1997; Gladders et al. 1998; Smail et al. 1998; Bell et al. 2004) as well as scaling relations between velocity dispersion and the strengths of absorption lines (e.g. Bender et al. 1993; Jørgensen 1997; Colless et al. 1999). It has

Electronic address: jmb@astro.ox.ac.uk
 Electronic address: rld@astro.ox.ac.uk
 Electronic address: ijorgensen@gemini.edu
 Electronic address: mbergmann@noao.edu
 Electronic address: david.crampton@nrc.ca

been claimed that such correlations imply that the cluster population shares a common, often quiescent, star formation history. This must be reconciled with observations of galaxy clusters which show complex processes such as mergers, bursts of star formation and interactions involving powerful active galaxies (e.g. Fabian et al. 2000; Kempner et al. 2002; Sakai et al. 2002; Owen et al. 2005).

In order to constrain the star-formation history in clusters it is desirable to make observations at a number of epochs, and thus directly examine the scaling relations as a function of redshift. There are a growing number of studies which aim to do this (e.g. van Dokkum & Franx 1996; Ziegler & Bender 1997; Bender et al. 1998; Jørgensen et al. 1999; Kelson et al. 2000; van Dokkum et al. 2001; Ziegler et al. 2001; Andreon et al. 2004; Wuyts et al. 2004). For the most part, these investigations find that the amount of evolution in a particular observable from distant clusters to a nearby reference sample is consistent with pure passive evolution. This means that changes can be explained entirely by a stellar population created instantaneously at high redshift (typically $z_{\text{form}} > 2$) and evolving with no new star formation.

Until recently these studies typically sampled ~ 10 galaxies per cluster over a narrow range in luminosity from the red sequence. This restricts the analysis to a narrow range in galaxy mass, and so the dependence of a particular property on mass cannot be examined. Furthermore, observing only early-type galaxies does not account for morphological differences between distant and nearby clusters. It has been shown that between $z = 0.5$ and $z = 0$, a significant portion of the spiral galaxies in clusters become E and S0 galaxies (Dressler et al. 1997; van Dokkum et al. 2001). This means that any study which intends to address changes in clusters will have to avoid this so called “progenitor bias” by sampling the galaxy population as a whole rather than a potentially evolving subset.

In this work we present photometric and spectroscopic analysis of the stellar populations in RXJ0142.0+2131, a galaxy cluster at $z = 0.28$. It is the first of two papers on RXJ0142.0+2131: Hubble Space Telescope (*HST*) observations will be detailed in a future study (Barr et al., in preparation). The present paper is itself second in a series based on observations made as part of the Gemini/HST Galaxy Cluster Project, targeting the stellar populations in massive clusters of galaxies. The Gemini/HST Galaxy Cluster Project sets out to address the issues described above by observing 30–50 cluster members in 15 galaxy clusters in the $0.2 < z < 1$ interval. This is accomplished through *HST* imaging and deep spectroscopy from the twin 8m Gemini telescopes, and using recent single stellar population (SSP) models to derive luminosity-weighted mean ages, metallicities and α -element abundance ratios. The main science aims of the project are outlined in Jørgensen et al. (2005; hereafter J05). Details of the galaxy clusters observed as part of Gemini/HST Galaxy Cluster Project will be published in a future paper (Jørgensen et al., in preparation); the intent is to study massive clusters of galaxies over a redshift interval approximately equal to half the age of the universe. Clusters in the Gemini/HST Galaxy Cluster Project are selected from a variety of surveys to be representative of the population with $L_X \geq 2 \times 10^{44}$ erg

s⁻¹.

We use data from three low-redshift clusters as a control sample. These have been chosen based on the similarity of data quality and content. Photometry and velocity dispersions for 116 galaxies in the Coma cluster ($z = 0.023$) comes from Jørgensen (1999). Velocity dispersions and line indices from 63 galaxies in the Perseus cluster ($z = 0.018$) and 17 galaxies in Abell 194 ($z = 0.018$) are also used. The comparison galaxies lie on the red sequence and are classified as E or S0. There are no discernible offsets in the average measured properties of stellar populations in these three clusters. See J05 for further details. The full low-redshift comparison sample will be published in a future paper (Jørgensen 2005, in preparation).

In order to quantify further the changes in observables between $z = 0.28$ and $z \sim 0$, we use the models of Thomas et al. (2003a, 2004). They derive the line indices in the Lick/IDS system for stellar populations with varying age, metallicity ($[M/H]$), and α -element abundance ratio ($[\alpha/Fe]$). These are combined with the mass-to-light ratios (M/L) of Maraston (2004), the derivation of which employs the Thomas models. For non-Lick indices we also adopt models from Vazdekis (1997), and Bruzual & Charlot (2003) though these provide only for a solar $[\alpha/Fe]$. We investigate how the luminosities and values of line indices differ for galaxies in RXJ0142.0+2131 compared with the low-redshift comparison sample. We also make predictions of how these quantities would evolve from $z = 0.28$ to $z \sim 0$ assuming pure passive-evolution with a formation redshift of $z_{\text{form}} \simeq 2$. This formation redshift is implicit when we say “assuming passive evolution”, or “the passive evolution model”. Furthermore, any predicted changes in line index measurements within this scheme are due solely to changes in the luminosity-weighted mean ages of the stellar population. See J05 for an in-depth description of the application of the SSP models as part of the Gemini/HST Galaxy Cluster Project.

Previous observations of RXJ0142.0+2131 are summarised in Section 2. Section 3 outlines the observations and data reduction on which this paper is based. The analysis of derived kinematic and absorption-line quantities is the subject of §4, while implications are discussed in §5. Conclusions are presented in §6. Our adopted cosmology is $H_0 = 70$ km s⁻¹ Mpc⁻¹, $\Omega_m = 0.3$, $\Omega_\Lambda = 0.7$.

2. RXJ0142.0+2131: BACKGROUND INFORMATION

RXJ0142.0+2131 was first identified as a bright extended X-ray source in the ROSAT All Sky Survey (Voges et al. 1999) and subsequently as a massive cluster of galaxies at $z = 0.280$ in both the Northern ROSAT All-Sky Galaxy Cluster Survey (Böhringer et al. 2000) and the ROSAT extended Brightest Cluster Sample (Ebeling et al. 2000)¹. Its X-ray luminosity is $L_X(0.1 - 2.4 \text{ keV}) = 6.40 \times 10^{44}$ erg s⁻¹ in the cluster rest frame. There have been no *Chandra* or *XMM-Newton* observations so no information on the morphology of the cluster X-ray gas is available.

¹ The redshift of RXJ0142.0+2131 in Böhringer et al. (2000) is mistakenly given as 0.0696, which is the redshift of the bright, foreground spiral. The correct redshift is given in Ebeling et al. (2000).

TABLE 1
INSTRUMENTATION

Telescope	Gemini North
Instrument	GMOS-N
CCDs	3 × EEV 2048 × 4608
Read-out noise ^a	(3.5, 3.3, 3.0) e ⁻
gain ^a	(2.10, 2.34, 2.30) e ⁻ /ADU
Pixel scale	0''.0727/pixel
Field of view	5'.5 × 5'.5
Imaging filters	<i>g'</i> , <i>r'</i> , <i>i'</i>
Grating	B600-G5303
Slit width	0''.75
Slit length	4''.0 – 15''.0
Extraction aperture	0''.75 × 1''.2
<i>r_{ap}</i> ^b	0''.55
Spectral resolution, σ ^c	1.464 Å
Wavelength range ^d	4000–7500 Å

^aValues for the three detectors in the array^bEquivalent circular aperture; see Jørgensen et al. (1995)^cMedian of the instrumental resolutions, σ , measured for each slit from Gaussian fits to the sky lines. Note that this is equivalent to 73 km s⁻¹ measured at 4800 Å in the rest frame of RXJ0142.0+2131^dThe exact wavelength range varies from slit to slitTABLE 2
IMAGING OBSERVATIONS

Filter	Total exposure time (s)	Image quality FWHM (")	Sky brightness (mag arcsec ⁻²)
<i>g'</i>	6 × 600	0.67	21.45
<i>r'</i>	8 × 300	0.52	20.56
<i>i'</i>	8 × 300	0.53	19.87

3. OBSERVATIONAL DATA

Imaging and spectroscopy of RXJ0142.0+2131 were obtained with the Gemini Multi-Object Spectrograph on Gemini North (GMOS-N) in semester 2001B as part of GMOS-N System Verification program, GN-2001B-SV-51. See Hook et al. (2004) for a description of GMOS-N. Observations were made within the period UT 2001 October 20 to 2001 November 18. Table 1 gives the instrumental setup, Tables 2 and 3 summarise the imaging and spectroscopic observations respectively. The spectroscopic observations were obtained as 18 individual exposures of 1800s, split between two masks. Because some objects appear in both masks, exposure times differ according to object, and vary from 4 to 9 hours.

The basic reduction of the data was made using a combination of the Gemini IRAF² package and custom reduction techniques written in IRAF. Details of these routines are given either in this paper or in J05 which contains a thorough, general description of both the photo-

TABLE 3
SPECTROSCOPIC OBSERVATIONS

Mask ID	Exposure time (s)	Image quality ^a		
		5000 Å (")	6000 Å (")	7000 Å (")
GN-2001B-SV-51-2	18000	0.72	0.79	0.70
GN-2001B-SV-51-3	14400	0.88	0.88	0.86

^aFWHM measured by fitting a Gaussian in the spatial direction to one of the alignment stars in the mask

metric and spectroscopic reduction processes applied to GMOS-N data. In the present work we outline the data reduction and expand only where the process differs from J05.

All data taken as part of GN-2001B-SV-51 are publicly available through the Gemini Science Archive (<http://cadwww.hia.nrc.ca/gemini/sv/>).

3.1. Derived photometric parameters

Broad-band images in *g'*, *r'*, and *i'* are reduced in standard fashion, as described in the Appendix. These images are then processed using the object detection and photometry package SExtractor (Bertin & Arnouts 1996). We use the *i'*-band image to detect objects which are then photometrically processed in each band individually. The catalogs are visually inspected as a final measure to ensure that galaxies are correctly separated from one another.

We adopt the best magnitudes (*mag_{best}*) from SExtractor as the total magnitude of the object. Colors are calculated from aperture magnitudes within a diameter of 1''.34, which is twice the seeing FWHM in the *g'*-band. From simulated model images of galaxies convolved with the relevant image quality we estimate the systematic effects on the colors due to the differences in image quality. There is no significant effect on the *r'*–*i'* colors. For the *g'*–*r'* and *g'*–*i'* colors, the effect is no more than 0.02. The uncorrected colors are systematically too red. This small effect does not significantly affect our analysis of the data. Magnitudes and colors in *r'* and *i'* are calibrated to rest-frame *B* for comparison with the low-redshift sample (see Appendix, § A.2).

The typical uncertainties on the magnitudes and colors of galaxies in the spectroscopic sample from photon noise alone are 0.002 mag and 0.003 mag respectively. This does not account for uncertainties introduced by the reduction pipeline. The effect on the uncertainties in magnitude and color due to the photometric reduction is assessed in J05. For *i'* < 21.5 typical uncertainties are 0.035 mag in magnitude and 0.045 mag in color, while for 21.5 < *i'* < 22.5 the values are 0.06 and 0.07.

We separate galaxies into “bulge-like” or “disk-like” by analysing their surface photometry in the GMOS-N *r'*-band using GALFIT³ (Peng et al. 2002). The GALFIT program fits various types of two-dimensional luminosity profiles to data. GALFIT is used to fit each galaxy in the spectroscopic sample as a Sérsic profile (Sérsic 1968) and find the best-fitting power-law index, *n*. We use this

² IRAF is distributed by the National Optical Astronomy Observatories, which are operated by the Association of Universities for Research in Astronomy, Inc. (AURA), under cooperative agreement with the National Science Foundation. The Gemini IRAF package is distributed by Gemini Observatory, which is operated by AURA.

³ <http://zwicky.as.arizona.edu/~cyp/work/galfit/galfit.html>

determination in a relative sense to distinguish bulge-like from disk-like and arbitrarily define anything with $n \geq 2$ as a bulge-like galaxy.

3.2. Spectroscopic data – sample selection

The spectroscopic sample was selected based on the photometry. Stars and galaxies were separated using the SExtractor classification parameter *class_star* derived from the image in the i' -filter. At the time of the sample selection for RXJ0142.0+2131 we were using a threshold of 0.90, i.e., objects with *class_star* < 0.90 in the i' -image are considered galaxies. For clusters observed later in the project, we used 0.80. The effect of this is discussed below.

Selection categories were set based on the total magnitude in r' and the colors. We used a color selection that includes all likely cluster members. The categories were set as follows.

- 1: $r' \leq 19.4 \wedge 1.8 \leq (g' - i') \leq 2.4 \wedge (r' - i') \leq 0.7$
- 2: $19.4 < r' \leq 21.2 \wedge 1.8 \leq (g' - i') \leq 2.4 \wedge (r' - i') \leq 0.7$
- 3: $19.4 < r' \leq 21.2 \wedge 1.0 \leq (g' - i') < 1.8$
- 4: $(r' \leq 21.2 \wedge (g' - i') < 1.0) \vee (r' \leq 21.2 \wedge ((g' - i') > 2.4) \vee (r' - i') > 0.7) \vee (21.2 < r' \leq 21.6 \wedge 1.0 \leq (g' - i') \leq 2.4)$

Figure 1 summarises the photometry for the field as color-magnitude diagrams and color-color diagrams. The spectroscopic sample is marked, with cluster members as solid green boxes. The selection categories are visualized on Figure 1b. Positions and photometry for the spectroscopic sample are given in Table A7.

All objects included in categories 1, 2, and 3 were also required to meet the condition

$$(r' - i') \leq 0.7 \wedge 1.0 \leq (g' - i') \leq 2.4 \wedge$$

$$(g' - i) \leq 4 \cdot (r' - i') \wedge (g' - i) \geq 3.2 \cdot (r' - i') - 0.44$$

This condition corresponds to the area outlined on Figure 1c.

Category 1 and 2 objects are the most important to include in the spectroscopic sample. Roughly the same number of galaxies from each of these categories were included in the final spectroscopic sample. Category 3 objects, which are likely to include blue cluster members, are included whenever no category 1 or 2 object is available. Due to the distribution of the category 1, 2 and 3 objects in the field, not all of the available space on the masks could be filled. We therefore included category 4 objects in order to fill both masks. The very blue category 4 objects are expected to be foreground galaxies, while the very red category 4 objects may be background galaxies. The faint category 4 objects are expected to include cluster members.

The star-galaxy classification parameter *class_star* in the i' -filter is 0.01-0.04 for all the objects in the spectroscopic sample, except for one object which has *class_star* = 0.88 and turned out to be an M star. If we had used the criteria *class_star* < 0.80 as done for other clusters in

the Gemini/HST Galaxy Cluster Project, this star would not have been included in the sample. However, its inclusion has not significantly changed the sample selection, since only one other possible cluster member would have been observed instead.

The M star is the only category 1 non-member. There are two faint category 2 non-members. Four of the nine category 3 galaxies observed were non-members, while all the very blue and very red category 4 galaxies were non-members. Of the three faint category 4 galaxies observed, two are members of RXJ0142.0+2131. Figure 2 shows the r' -band image with the spectroscopic sample marked.

3.3. Derived spectroscopic parameters

Flux-calibrated one- and two-dimensional spectra are produced for each object as described in the Appendix (§ A.3), which follows the method in J05.

Redshifts, velocity dispersions and line indices are derived from the extracted 1D spectra. For galaxies with emission lines, the initial redshift estimates are made using these. Otherwise, the spectrum is cross-correlated with that of the K0III star HD172401, using the IRAF tasks *fxcor* and *xcsao*.

With the redshift determined to $\pm 200 \text{ km s}^{-1}$, more accurate kinematic parameters are determined using spectral-fitting software written by Karl Gebhardt (Gebhardt et al. 2000; 2003; see also Saha & Williams 1994; Merritt 1997); see J05 for a description of how this program is adapted to deal with intermediate-to-high redshift spectra. The program simultaneously fits the kinematics and optimises the template mix in pixel space using a maximum penalised likelihood (MPL) method. The templates are constructed from three stars observed with GMOS-N to prevent systematic errors being introduced by template mismatch. The observations of the template stars are detailed in J05.

For each galaxy, the spectrum is normalised (using a 27-piece cubic spline, rejecting points $\pm 3\sigma$ from the fit), shifted to the rest frame and cut to the wavelength covered by both galaxy and template stars. Emission lines and sky residuals are masked. In most cases the fits are from 3750–5400 Å in the rest frame with exceptions being where the S/N is too low at the blue end to be of any use. The best fit is then determined using the MPL technique. Uncertainties are estimated from Monte Carlo simulations. Values of velocity dispersion, refined redshift and template fractions are returned. The latter information can be used to give an estimate of the spectral classification for the galaxy. Velocity dispersions calculated from the template fitting are corrected to an aperture of $3''.4$ at the redshift of the Coma cluster according to the prescription of Jørgensen et al. (1995). The results of the template fitting are shown in Table B8.

We derive the absorption line indices CN₂, G4300, C4668, Mgb, Fe5270 and Fe5335 (Combined as $\langle \text{Fe} \rangle^4$) from Worthey et al. (1994) on the Lick/IDS system. We also derive H β _G (González 1993; Jørgensen 1997), the higher-order Balmer lines H γ _A and H δ _A (Worthey & Ottaviani 1997), the D4000 index (Bruzual 1983; Gorgas et al. 1999) and the blue indices CN3883 and CaHK (Davidge & Clark 1994). Line indices are determined from spectra convolved to the in-

⁴ $\langle \text{Fe} \rangle = 0.5(\text{Fe}5270 + \text{Fe}5335)$

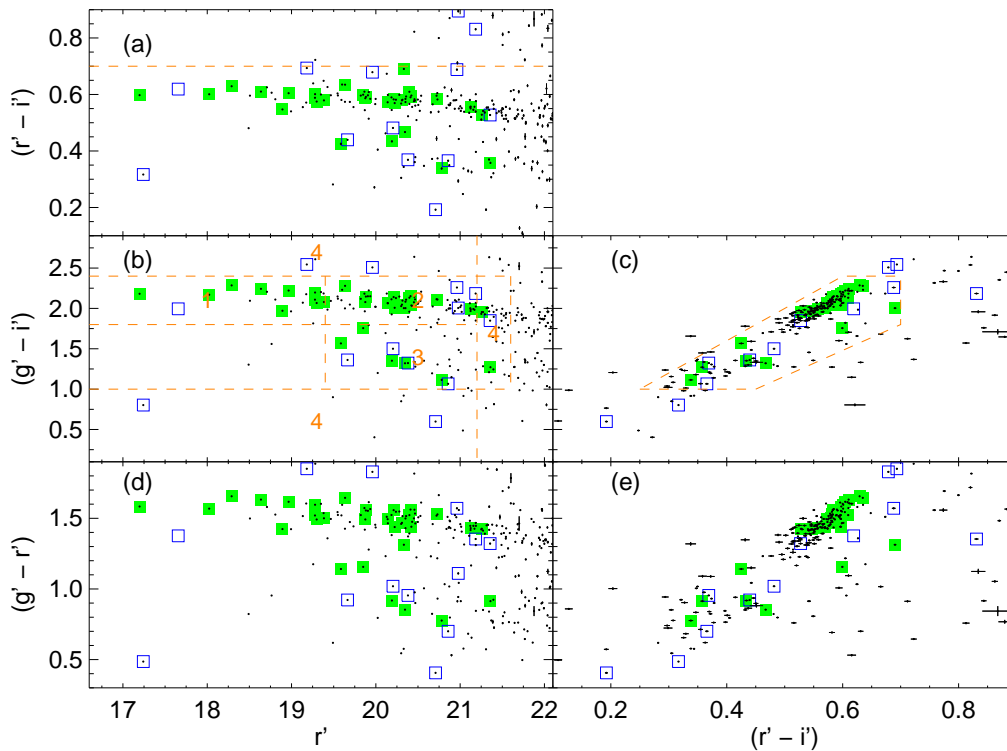


FIG. 1.— RXJ0142.0+2131: Color-magnitude and color-color diagrams. Objects with $class_star \leq 0.80$ and $r' \leq 22.1$ are marked with points and error bars. Boxes indicate those objects in the spectroscopic sample. Filled boxes are confirmed cluster members. The dashed lines show the magnitude- and color-based selection criteria and categories used in assigning spectroscopic targets are shown in the $(g' - i')$ vs. r' plot. The open box without a corresponding point is the M star whose $class_star$ is 0.88 (see §3.2).

strumental resolution of the Lick/IDS system. They are then corrected for velocity dispersion using the technique described in Davies et al. (1993); see also J05. The zero-velocity indices are corrected to an aperture of $3''/4$ at the Coma cluster after Jørgensen (1997). See J05 for the adopted aperture corrections. No correction for spectral-shape differences between Lick/IDS and our spectra is made. Previous studies have shown these to be small, with uncertainties almost as large as the offsets themselves (e.g. Jørgensen 1997). The line indices for the spectroscopic sample are listed in Table B9. Note that we do not derive Fe4383 as residuals from the strong sky line at 5577\AA fall within the line band for cluster members. This sky line also affects some of the $H\gamma_A$ measurements. In these cases (IDs 322, 671, 1179, 1412) $H\delta_A + H\gamma_A$ was calculated using a linear relation between $H\delta_A$ and $H\delta_A + H\gamma_A$ derived from the other cluster members. There are also four cluster members which have accurate determinations of Fe5270 (IDs 116, 128, 1029, 1076), but for which Fe5335 either lies beyond the of spectral range or has a large error. For these objects we calculate $\langle Fe \rangle$ by assuming a linear relation between Fe5270 and $\langle Fe \rangle$ calibrated using those cluster members with both Fe5270 and Fe5335.

Of the 43 objects targeted for spectroscopic observations, 30 are found to be cluster members (see §4.1 and

Table B8), 12 are galaxies at other redshifts and one is an M star. Extracted 1D spectra of the galaxies are reproduced in the appendix, cluster members are shown in Figure B10 and non-members in Figure B11. GMOS-N color images of each galaxy in the form of postage stamps are shown in Figure B12 for cluster members and Figure B13 for non-members.

4. RESULTS & ANALYSIS

In this section, redshift information is used initially to determine cluster membership. We then examine the properties of the cluster as a whole, e.g. cluster velocity dispersion and richness, and search for substructure, before analysing diagnostics of the stellar populations of individual galaxies. When examining stellar populations we focus on the color-magnitude diagram, scaling relations involving the velocity dispersion, and absorption-line indices.

4.1. The cluster properties of RXJ0142.0+2131

In order to determine membership of RXJ0142.0+2131, we first exclude galaxies $\pm 3000 \text{ km s}^{-1}$ from the published redshift of 0.280. We then iteratively determine z_{cluster} and σ_{cluster} using the bi-weight distribution method (Beers et al. 1990). A total of 30 galaxies are classified as cluster members with a mean redshift of 0.2796 ± 0.0008 and velocity dispersion

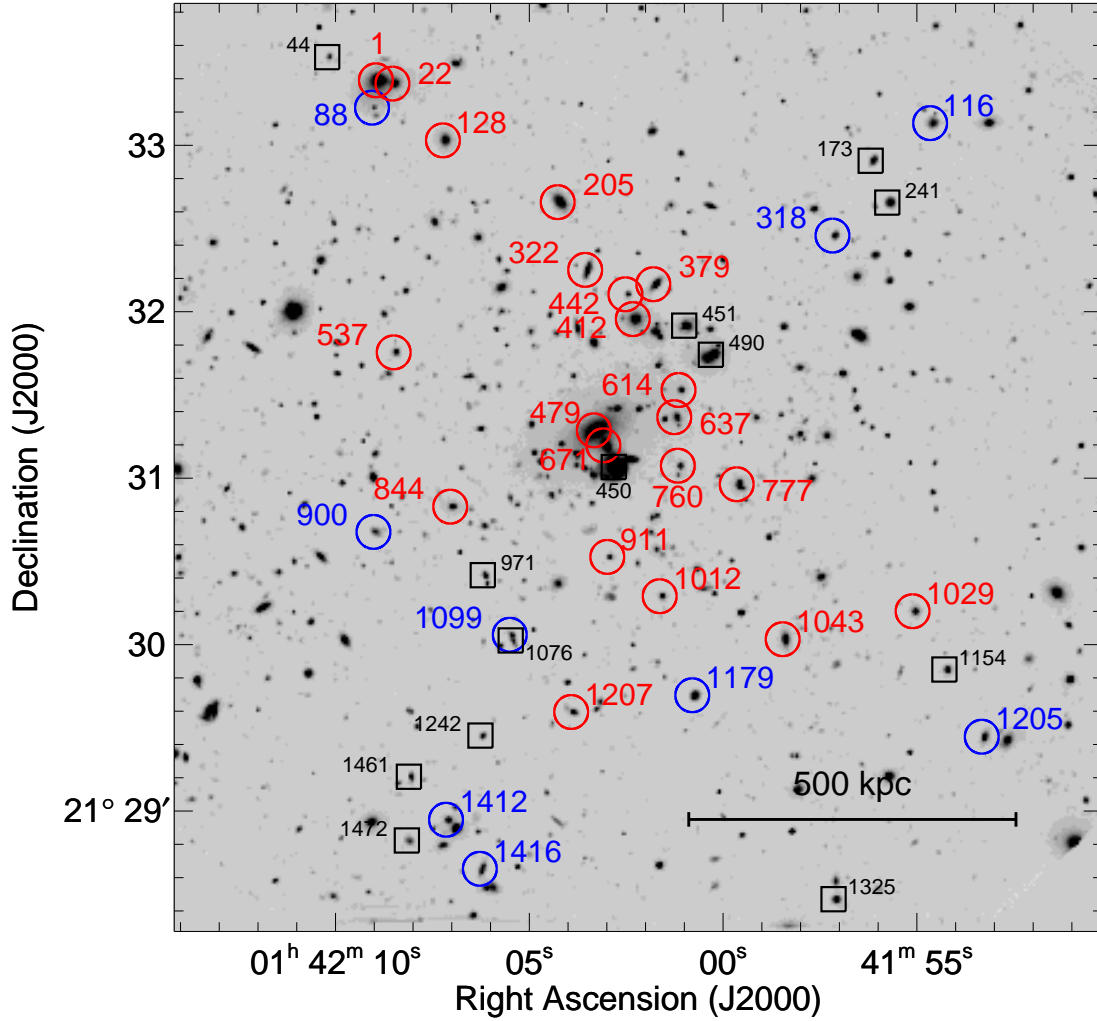


FIG. 2.— RXJ0142.0+2131 r' -band image with the spectroscopic sample marked. The field size is $5/5 \times 5/5$; North is up, East is left. Confirmed cluster members are marked with a circle, non-members with a square. Cluster galaxies are color coded according to morphology; red: bulge-like; blue: disk-like.

in the rest frame $1278 \pm 134 \text{ km s}^{-1}$. As a comparison, we also determine σ_{cluster} using the method of Danese et al. (1980). This yields a value of $1212^{+207}_{-143} \text{ km s}^{-1}$, which agrees with the biweight distribution estimate. The X-ray luminosity of RXJ0142.0+2131 is about 1.7 times that of Coma, which has a line-of-sight velocity dispersion of $1010^{+51}_{-44} \text{ km s}^{-1}$ (Zabludoff et al. 1990). If we assume that Coma lies on the $L_X - \sigma$ relation ($L_X \propto \sigma^{4.4}$) of Mahdavi & Geller (2001), we find that L_X in RXJ0142.0+2131 is fainter than predicted by 0.22 dex in $\log L_X$. The scatter in the Mahdavi & Geller relation is 0.18 dex in $\log L_X$. It would be unwise to draw firm conclusions on X-ray luminosity from observations made with ROSAT. *Chandra* and *XMM-Newton* observations of previously classified ROSAT clusters of galaxies have shown ROSAT X-ray flux values to be too high because of the effect of unresolved AGNs (e.g.

Donahue et al. 2003). We are therefore required to view the ROSAT flux measurement as an upper limit.

Figure 2 shows the spatial distribution of spectroscopically confirmed cluster members in RXJ0142.0+2131. Galaxies are coded according to whether their luminosity profiles in the r' -band are bulge-like or disk-like as described in §3.1. Bulge-like and disk-like galaxies are well separated spatially, as we might presume from a morphology-density relation (e.g. Dressler 1980). The brightest and second brightest cluster members (ID 479 and ID 1) are separated by $\sim 650 \text{ kpc}$, and the brightest cluster galaxy (BCG) is displaced by 1000 km s^{-1} from the systemic cluster redshift, which might suggest that RXJ0142.0+2131 is not fully virialized. However, the spatial distribution of red-sequence galaxies as a whole shows no obvious substructure projected on the sky.

The velocity distribution of cluster members is shown

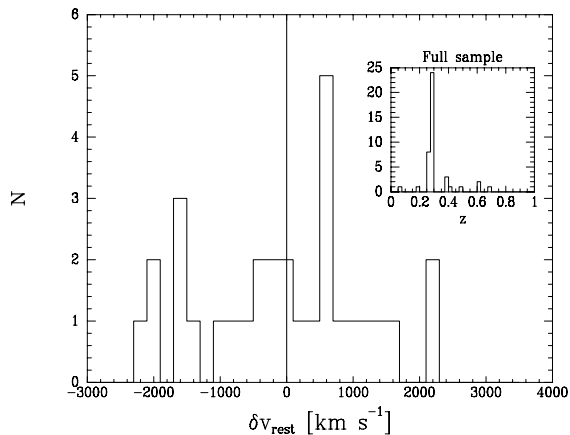


FIG. 3.— Rest-frame velocity distribution for cluster members. The inset shows the redshift distribution of the spectroscopic sample.

in Figure 3. A one-sided Kolmogorov-Smirnov test shows the probability that the data are drawn from a Gaussian distribution is greater than 75%. We can also search for substructure using the method of Dressler & Shectman (1988) which identifies deviations in the velocities of galaxies and their projected neighbours from the cluster as a whole. The statistic returned (Δ) is χ^2 -like in that a Gaussian distribution returns a value of Δ which is of order of the number of degrees of freedom. For RXJ0142.0+2131, $\Delta = 28.9$. In order to quantify more properly the significance of this statistic we perform a Monte Carlo analysis on 1000 alternative realisations of the data. In each case the velocities are shuffled randomly and reassigned and the statistic is recalculated. We find that a higher value of Δ is found in $> 40\%$ of the artificial realisations implying that substructure is not significant in RXJ0142.0+2131.

In order to estimate the richness of RXJ0142.0+2131, we determine the galaxy-cluster spatial cross-correlation amplitude (B_{gc}) of Yee & López-Cruz (1999). B_{gc} quantifies the excess number of objects within 0.5 Mpc of the BCG, and attempts to introduce some redshift independence by normalising by an integrated luminosity function. See Seldner & Peebles (1978) and Longair & Seldner (1979) for a full derivation of this quantity. We employ luminosity functions from Wold et al. (2000). In the absence of control observations of blank fields, we use the area outside 0.5 Mpc of the BCG to determine a “field density”. This means we may overestimate the background where cluster members extend further than 0.5 Mpc from the BCG. However, we note that photometric data from the Coma cluster (Jørgensen, in preparation) give $B_{gc}(\text{Coma}) = 976 \pm 109 h_{50}^{-1.8} \text{ Mpc}^{-1.8}$, which is in agreement with the value of $1242 \pm 282 h_{50}^{-1.8} \text{ Mpc}^{-1.8}$ published in Yee & López-Cruz (1999). We find $B_{gc}(\text{RXJ0142.0} + 2131) = 637 \pm 132 h_{50}^{-1.8} \text{ Mpc}^{-1.8}$.

Yee & Ellingson (2003) give the relationship between B_{gc} and cluster velocity dispersion for galaxy clusters at $0.2 < z < 0.5$. They find that the two quantities are well correlated over $500 < B_{gc} < 2000$. Our determinations of velocity dispersion and B_{gc} for RXJ0142.0+2131 indi-

cate that it is an outlier, with velocity dispersion around twice the expected value. We must be cautious with this result as we know that the estimation of the surface density of background galaxies may cause B_{gc} to be too low. However, to make the $B_{gc}(\text{RXJ0142.0} + 2131)$ consistent with the Yee & Ellingson prediction of $B_{gc} \simeq 2250$ we would have to reduce our estimated background surface density by a factor of 20. We consider such an overestimate highly unlikely as it implies a galaxy surface density of only $\sim 500 \text{ deg}^{-2}$ down to a magnitude of $r' = 23$, a factor of ~ 50 lower than that found by deep wide-field surveys (see e.g. Postman et al. 1998; Wilson 2003).

We also calculate the fraction of blue galaxies (f_B) in RXJ0142.0+2131 following Butcher & Oemler (1984). In order to make a fair comparison, we convert our r' and $g'-r'$ quantities into V and $B - V$ via the relations of Smith et al. (2002). Butcher & Oemler define f_B as the fraction of galaxies with $M_V < -20$ and $B - V$ 0.2 mag bluer than the red sequence. We note that there are two aspects of the calculation that are difficult to reproduce. Firstly, f_B is calculated in the radius within which 30% of the cluster galaxies are contained (R_{30}). We find it difficult to determine this quantity for RXJ0142.0+2131, because the cluster is not strongly concentrated, and our field-of-view is too small to permit an estimate of the cluster’s extent. We therefore take R_{30} to be equal to the median R_{30} found by Butcher & Oemler for clusters with $0.2 < z < 0.4$. This gives us $R_{30}(\text{RXJ0142.0} + 2131) = 2/4$, but we note that the value of f_B remains consistent if R_{30} is changed by ± 0.5 . More important is the correction applied to account for foreground and background galaxies. We make this adjustment, in the same way as for B_{gc} , by assuming that the galaxies at projected distances greater than 0.5 Mpc from the BCG can be taken as representative of the field. We use these galaxies to determine the expected number of galaxies within R_{30} , centred on the BCG, with $M_V < -20$ and $B - V$ 0.2 mag bluer than the red sequence.

We find that $f_B(\text{RXJ0142.0} + 2131) = 0.22 \pm 0.06$. This is consistent with the $f_B - z$ measurements of Butcher & Oemler (1984) and Fairley et al. (2002) for clusters at $z \simeq 0.28$. How this figure is affected by contamination of the background by cluster galaxies depends on the ratio of blue and red galaxies at > 0.5 Mpc from the BCG, and their relative numbers when compared with the background. It is quite difficult to gauge this effect. However, we note that the blue fraction of these “background” galaxies is 0.45 ± 0.08 , consistent with the Butcher & Oemler determination of the field.

The analyses of cluster velocity dispersion, X-ray luminosity, richness, and blue fraction employ no spectroscopic information other than redshift. As such they form only a prelude to the real meat of this paper. Nevertheless, they suggest that RXJ0142.0+2131 has a higher σ_{cluster} than both its X-ray luminosity and optical richness would suggest, and its blue fraction is as expected from its redshift. These phenomena are examined further in the context of stellar populations in §5.

4.2. The color-magnitude diagram

We compare the slope and zero-points of the red sequence of our GMOS-N spectroscopic sample with the predictions of Kodama & Arimoto (1997) for a cluster of galaxies at $z = 0.28$. Kodama & Arimoto conclude

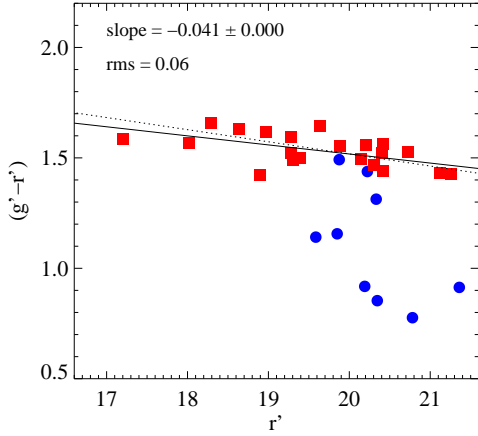


FIG. 4.— Color-magnitude diagram for spectroscopically-confirmed members of RXJ0142.0+2131. Squares represent bulge-like galaxies, circles are the disk-like members (see the text for a description of how these are defined). The solid line is an iterative fit to red-sequence galaxies (see text), and the dotted line is the predicted $(g' - r')$ vs. r' red sequence at $z = 0.28$ for a passively-evolving elliptical population formed at $z_{\text{form}} \simeq 2$ from Kodama & Arimoto (1997).

that the presence of a cluster red sequence at all redshifts can be explained if ellipticals have a common formation epoch, $z_{\text{form}} \simeq 2$, and evolve passively. The slope of the red sequence is caused by fainter galaxies having lower metallicities; the timescale for the loss of metals via a galactic wind is shorter for less massive galaxies. Their $[M/H]$ values range from 0.15 to -0.37 over $-22 < M_B < -18$ for a 15 Gyr old galaxy. More usefully, Kodama & Arimoto give the evolution of elliptical galaxies on the $(g - r)$ vs. r color-magnitude diagram (CMD) with redshift. We compare their red sequence at $z = 0.28$ with our data.

The $(g' - r')$ vs. r' color-magnitude diagram for RXJ0142.0+2131 is shown in Figure 4. The slope and intercept of the red sequence are calculated by making a least-squares fit to the cluster members with $(g' - r') > 1$, iteratively rejecting points that deviate from the fit by more than 3σ . The predicted red sequence of a cluster of galaxies at $z = 0.28$ (Kodama & Arimoto 1997) is the dotted line. The model agrees with the observed red sequence, indicating that the colors of bulge-like galaxies in RXJ0142.0+2131 are consistent with a passively-evolving population formed at $z_{\text{form}} \simeq 2$.

Figure 4 shows cluster members divided according to morphology. The bulge-like and disk-like galaxies are well separated; only two of the latter appear on the red sequence. It is important to note that the morphological determination is independent of color – we do not assume that disk-like galaxies belong in the blue population, or vice-versa. As noted in the previous section, the two populations are also separated spatially.

4.3. Correlations with velocity dispersion

We now investigate how the luminosities and absorption line strengths of galaxies in RXJ0142.0+2131 vary with the central velocity dispersion, and in particular if these relationships are the same as those in the low-

redshift sample. The indices' dependence on age, metallicity and $[\alpha/\text{Fe}]$ are calculated using the SSP models of Thomas et al. (2003a, 2004), Maraston (2004), Vazdekis (1997), and Bruzual & Charlot (2003). The models provide $H\beta$ which is converted to $H\beta_G$ using the transformation from Jørgensen (1997). See J05 for a full description of the derivation of these scaling relations. Table 4 outlines the predicted behavior of the indices used in this paper with age, metallicity and $[\alpha/\text{Fe}]$.

The scaling relations for RXJ0142.0+2131 and the comparison sample are shown in Table 5 and Figures 5 and 6. Note that the values of M_B come from the Coma cluster, whereas values of line indices, with the exception of $H\beta_G$, Mgb , and $\langle \text{Fe} \rangle$, are those of Perseus and Abell 194. The differing spectral range of the individual spectra mean that not all indices can be derived for all objects. For this reason the number of points in Figures 5 and 6 differs from panel to panel.

We determine the scaling relations by fitting a linear relation to the local galaxies. The corresponding relation for RXJ0142.0+2131 is quantified as the median offset of the galaxies in RXJ0142.0+2131, preserving the slope. Linear fits to the low-redshift sample are made by minimising the sums of the absolute residuals in the direction perpendicular to the slope. Uncertainties in the slopes are calculated using a bootstrap method. The zero points are derived by fitting to the median of the measurements. This method has been shown to be very robust to outliers. We quantify the random uncertainties in the zero points ($\sigma_{\Delta\gamma i}$), and also the uncertainty due to possible systematic effects in the determination of the velocity dispersion ($\sigma_{\text{sys } i}$). The latter quantity is based on the systematic uncertainty of 0.026 in $\log \sigma$, as derived in J05. The total uncertainty in the relation is equal to $\sigma_{\Delta\gamma i} + \sigma_{\text{sys } i}$. For $H\delta_A + H\gamma_A$ vs. $\log \sigma$ we adopt the slope, determined by Kelson et al. (2001), of CL1358+62 at $z = 0.33$. The zero point in this case is the median value of $H\delta_A + H\gamma_A$ of the low-redshift galaxies.

When determining the relationships for RXJ0142.0+2131, we exclude those cluster members with obvious emission-lines, indicated in Table B9. We also exclude the galaxies with $\sigma_{\log \sigma} > 0.1$. The comparison in this section is therefore between E and S0 galaxies in the local sample and galaxies within 0.2 mag of the red sequence in RXJ0142.0+2131.

Figure 5 plots age-dependant observables against velocity dispersion. Figure 5a is the FJ relation between rest-frame B -band magnitude and velocity dispersion. A cursory examination of the distribution of velocity dispersions in each sample indicates that RXJ0142.0+2131 lacks high- σ galaxies. This can be seen with most emphasis in Figure 5b and Figures 6a and 6b. Furthermore, there are only 2 red-sequence galaxies within 1.5 mag of the BCG magnitude not selected for spectroscopy (see Figure 1). This suggests that the paucity of high- σ galaxies is real, not a function of our spectroscopic selection. The FJ relation shows that the BCG in RXJ0142.0+2131 has conspicuously low velocity dispersion for its luminosity. The scatter in the RXJ0142.0+2131 points is larger than that of the control sample and the offset is consistent with that expected from passive evolution of the galaxy population within the errors. A more accurate measure of the luminosity evolution can be made when the parameters are better constrained by the FP, and

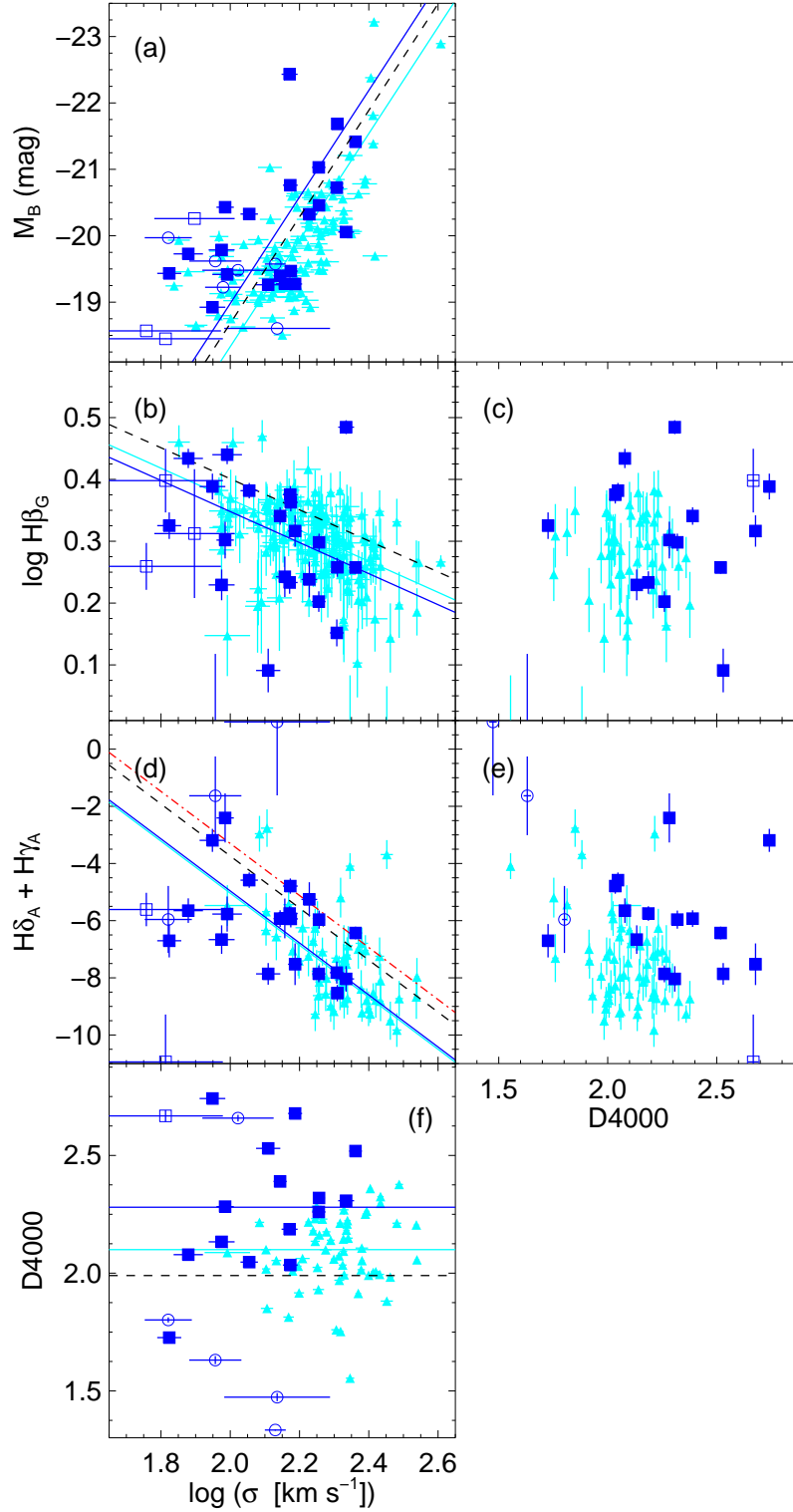


FIG. 5.— Scaling relations for age-dependant indices. (a) is the Faber-Jackson relation for RXJ0142.0+2131. Triangles are galaxies from the low-redshift comparison sample. The light blue solid line is the linear fit to these points as described in the text. Boxes are galaxies in RXJ0142.0+2131 with no emission lines, circles are emission-line galaxies. The dark blue solid line is the fit to the non-emission-line galaxies in RXJ0142.0+2131 preserving the low-redshift slope (see text). Those points excluded from the fit are plotted as open boxes. The relationship expected for passively-evolving galaxies at $z = 0.28$, with a formation redshift of $z_{\text{form}} = 2$ is indicated by the dashed line. The red dot-dashed line is the relationship found by Kelson et al. (2001) for a cluster of galaxies at $z = 0.33$.

TABLE 4
PREDICTIONS FROM SINGLE STELLAR POPULATION MODELS

Relation		rms	Reference
$\log M/L_B$	$= 0.935 \log \text{age} + 0.337[M/H] - 0.053$	0.022	Maraston 2004
$\log H\beta_G$	$= -0.221 \log \text{age} - 0.114[M/H] + 0.055[\alpha/\text{Fe}] + 0.500$	0.010	Thomas et al.
$(H\delta_A + H\gamma_A)'$	$= -0.115 \log \text{age} - 0.095[M/H] + 0.095[\alpha/\text{Fe}] + 0.009$	0.008	Thomas et al. ^a
D4000	$= 0.730 \log \text{age} + 0.711[M/H] + 1.827$	0.052	Vazdekis-2000
$\log Mgb$	$= 0.173 \log \text{age} + 0.309[M/H] + 0.210[\alpha/\text{Fe}] + 0.354$	0.019	Thomas et al.
$\log \langle \text{Fe} \rangle$	$= 0.113 \log \text{age} + 0.253[M/H] - 0.278[\alpha/\text{Fe}] + 0.343$	0.007	Thomas et al.
$\log C4668$	$= 0.145 \log \text{age} + 0.581[M/H] + 0.023[\alpha/\text{Fe}] + 0.529$	0.037	Thomas et al.
CN ₂	$= 0.121 \log \text{age} + 0.196[M/H] + 0.066[\alpha/\text{Fe}] - 0.043$	0.025	Thomas et al.
$\log CaHK$	$= 0.073 \log \text{age} + 0.061[M/H] + 1.291$	0.010	Bruzual & Charlot 2003
CN3883	$= 0.173 \log \text{age} + 0.142[M/H] + 0.086$	0.012	Bruzual & Charlot 2003
$\log G4300$	$= 0.162 \log \text{age} + 0.163[M/H] + 0.114[\alpha/\text{Fe}] + 0.552$	0.029	Thomas et al.

NOTE. — (1) Relation established from published model values. $[M/H] \equiv \log Z/Z_\odot$ is the total metallicity relative to solar. $[\alpha/\text{Fe}]$ is the abundance of the α -elements relative to iron, and relative to the solar abundance ratio. The age is in Gyr. M/L is the stellar mass-to-light ratio in solar units. (2) Scatter of the model values relative to the relation. (3) Reference for the model values.

^a $(H\delta_A + H\gamma_A)' \equiv -2.5 \log(1 - (H\delta_A + H\gamma_A)/(43.75 + 38.75))$, cf. Kuntschner (2000). The rms for the relation translates to an rms of $H\delta_A + H\gamma_A$ of ≈ 0.65 for the typical values of $H\delta_A + H\gamma_A$.

TABLE 5
SCALING RELATIONS

Relation		Low-redshift sample			RXJ0142.0+2131			$\Delta\gamma_i$	$\sigma_{\Delta\gamma\ i}$	$\sigma_{\text{sys}\ i}$	PE_i
(1)		γ_i (2)	N_{gal} (3)	rms (4)	γ_i (5)	N_{gal} (6)	rms (7)	(8)	(9)	(10)	(11)
M_B	$= (-8.02 \pm 1.08) \log \sigma + \gamma_i$	-2.29	116	0.81	-2.94	21	1.06	-0.65	0.24	0.21	-0.35
$\log H\beta_G$	$= (-0.25 \pm 0.05) \log \sigma + \gamma_i$	0.870	160	0.086	0.850	21	0.093	-0.020	0.021	0.007	0.033
$H\delta_A + H\gamma_A$	$= (-9.1 \pm 1.0) \log \sigma + \gamma_i^a$	13.16	65	1.53	13.24	21	3.74	0.08	0.84	0.24	1.30
D4000	$= \gamma_i$	2.10	65	0.16	2.28	15	0.26	0.18	0.07	...	-0.11
$\log Mgb$	$= (0.31 \pm 0.02) \log \sigma + \gamma_i$	-0.063	144	0.059	-0.022	21	0.098	0.041	0.022	0.008	-0.026
$\log \langle \text{Fe} \rangle$	$= (0.16 \pm 0.03) \log \sigma + \gamma_i$	0.103	144	0.053	0.096	20	0.049	-0.007	0.012	0.004	-0.017
$\log C4668$	$= (0.33 \pm 0.08) \log \sigma + \gamma_i$	0.107	65	0.058	0.117	20	0.150	0.010	0.034	0.009	-0.022
CN ₂	$= (0.22 \pm 0.06) \log \sigma + \gamma_i$	-0.390	65	0.034	-0.376	21	0.037	0.014	0.009	0.006	-0.018
$\log CaHK$	$= (0.14 \pm 0.04) \log \sigma + \gamma_i$	0.997	65	0.048	1.061	19	0.043	0.064	0.012	0.004	-0.011
CN3883	$= (0.30 \pm 0.04) \log \sigma + \gamma_i$	-0.431	65	0.051	-0.395	15	0.075	0.036	0.020	0.008	-0.026
$\log G4300$	$= (0.14 \pm 0.08) \log \sigma + \gamma_i$	0.403	65	0.051	0.437	20	0.058	0.034	0.014	0.004	-0.024

NOTE. — (1) Scaling relation. (2) Zero point for the low-redshift sample. (3) Number of galaxies in the low-redshift sample. (4) rms in the y direction of the low-redshift sample. (5,6,7) As 3,4,5 for the RXJ0142.0+2131 sample. (8) Zero point difference, $\gamma_i \text{ RXJ0142.0+2131} - \gamma_i \text{ low-}z$. (9) The statistical uncertainties are calculated as

$$\sigma_{\Delta\gamma_i} = (\text{rms}_{\text{low-}z}^2 / N_{\text{low-}z} + \text{rms}_{\text{RXJ0142.0+2131}}^2 / N_{\text{RXJ0142.0+2131}})^{0.5}.$$

(10) Systematic uncertainties on $\Delta\gamma_i$, derived as 0.026 times the coefficient of $\log \sigma$, based on the systematic uncertainties in $\log \sigma$ for the low-redshift sample. See J05 for more details. (11) Zero point difference as predicted by the relations in Table 4 and pure passive evolution.

^a Slope adopted from Kelson et al. (2001)

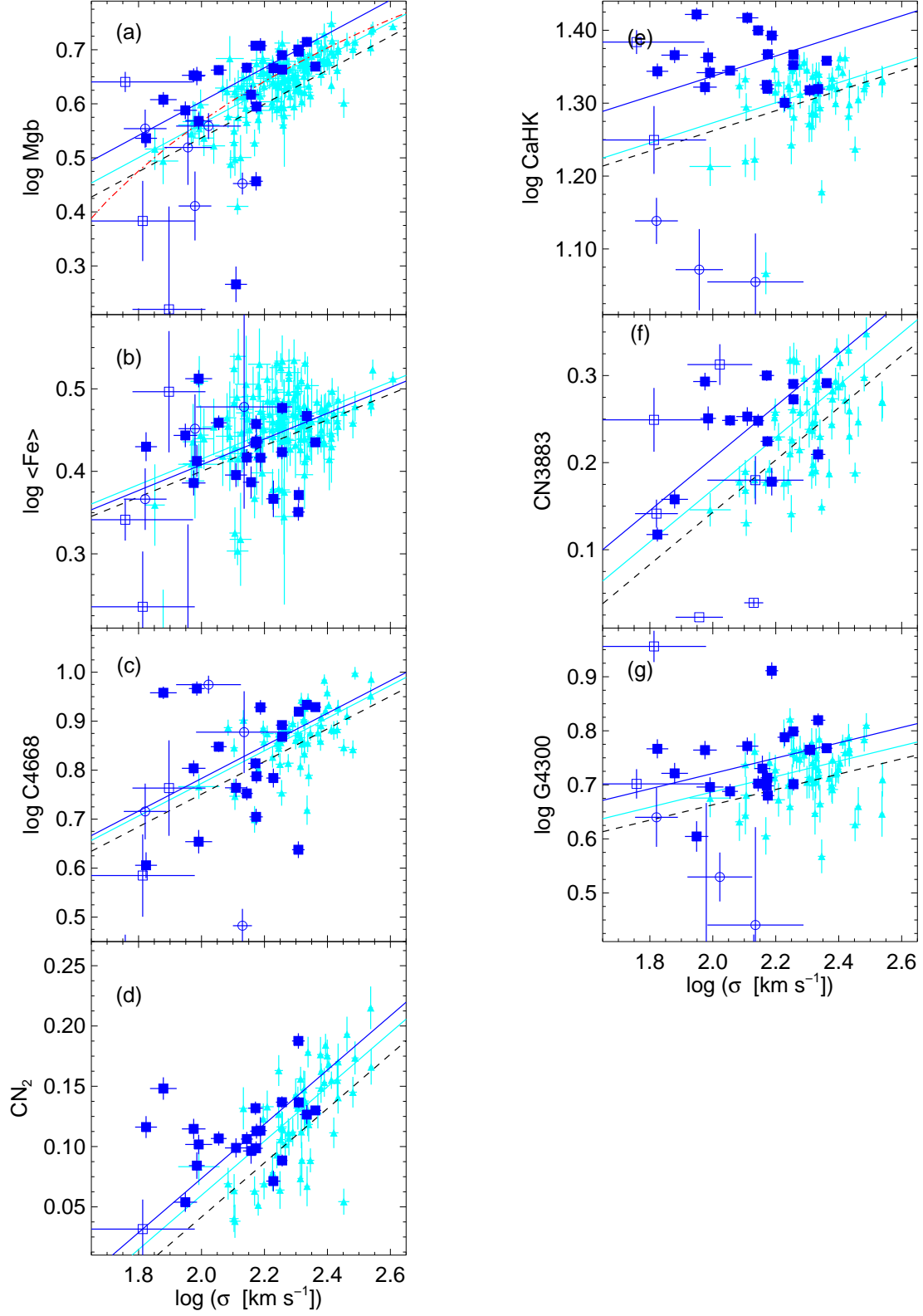


FIG. 6.— Scaling relations for the metal indices. The red dot-dashed line in (a) represents the relationship found by Colless et al. (1999) for cluster galaxies at $0.02 < z < 0.05$. All other plotting symbols and lines are as described in Figure 5.

hence will have to wait until *HST* observations of the surface brightnesses and effective radii are analysed (Barr et al., in preparation).

Figure 5b-f shows scaling relations for $H\beta_G$ and $H\delta_A + H\gamma_A$ and D4000. The Balmer line indices show marginal inconsistency with passive evolution, (1.4σ and 1.1σ respectively). The strength of the 4000Å break is uncorrelated with velocity dispersion (a Kendall's τ correlation test indicates that there is no significant correlation in either data set). The values for RXJ0142.0+2131 are also significantly offset from those in the comparison sample; a two-sided Kolmogorov-Smirnov test indicates that there is a $< 1\%$ chance that the two sets of D4000 measurements are drawn from the same parent distribution. Furthermore, passive evolution of galaxies in a cluster would predict that D4000 is stronger at lower redshift, in contrast to Figure 5d. Using the relationship in Table 5, we estimate that the median value of D4000 for non-emission-line galaxies is stronger than expected from the passive-evolution model at greater than 4 times the uncertainty. Because the 4000Å break is predicted to be stronger for older stellar populations, there are no models which allow for this offset to occur through passive evolution.

Figure 6 shows the scaling relations for metal indices. In the cases of $\langle Fe \rangle$ and C4668 the difference in the populations can be explained by age differences alone. However, in all other cases the relation is offset significantly in the opposite direction to that expected from passive evolution. We can quantify the average, normalised offset for N indices from passive evolution as,

$$\Delta\gamma_n = \frac{1}{N} \sum_i^N \frac{PE_i - \Delta\gamma_i}{PE_i}$$

where $\Delta\gamma_i$ is the offset of each index from the comparison sample, and PE_i is the passive evolution offset (see Table 5). The uncertainties are then,

$$\sigma_{\Delta\gamma_n} = \frac{1}{N} \sqrt{\sum_i^N \left(\frac{\sigma_{\Delta\gamma_i}}{PE_i} \right)^2}$$

and,

$$\sigma_{sys_n} = \frac{1}{N} \sum_i^N \frac{\sigma_{sys_i}}{|PE_i|}$$

with the total uncertainty equal to $\sigma_{\Delta\gamma_n} + \sigma_{sys_n}$ as before. The metal indices combined (excluding $\langle Fe \rangle$ and C4668) are stronger than predicted by the passive evolution model, with 5 times the uncertainty. This result is not driven by a single measurement as it still holds (at 3.7 times the uncertainty) if we exclude CaHK, the most discrepant index. If $\langle Fe \rangle$ and C4668 are included, the enhancement remains at 3.9 times the uncertainty.

With the exception of $\langle Fe \rangle$ and CaHK, the rms scatter in the relations is higher for RXJ0142.0+2131 than the low-redshift comparison sample. This is not due to higher measurement errors, as the median uncertainty for the line indices in the RXJ0142.0+2131 sample is generally lower than that of the comparison sample.

4.4. Age-metallicity- $[\alpha/Fe]$ indicators

Figure 7 shows the visible line indices and D4000 against one another. Model grids from Thomas et al. (2003a, 2004) are overlaid.

Figure 7b plots $H\beta_G$, an age indicator, against the quantity $[MgFe]'$, constructed by Thomas et al. (2003a)⁵ to be an index independent of $[\alpha/Fe]$. We can infer from this plot that the age and metallicity distributions of the low-redshift comparison sample and RXJ0142.0+2131 are similar. Figure 7g complements this analysis in that it probes $[\alpha/Fe]$ space where age and metallicity are degenerate. In this plane it can be seen that $[\alpha/Fe]$ is higher in RXJ0142.0+2131 than in the local galaxies.

We now derive values for luminosity-weighted mean age, metallicity and $[\alpha/Fe]$ from $H\beta_G$, Mgb and $\langle Fe \rangle$ using the models of Thomas et al. (2003a). We use $H\beta_G$, Mgb and $\langle Fe \rangle$ because these are generally the best studied indices (e.g. Jørgensen 1999; Trager et al. 2000), and are consistent with observations of globular clusters, i.e. systems that can truly be thought of as SSPs. However, caution must be exercised, and results cannot be interpreted as absolute values of the physical parameters. This can be seen from Figure 7, and in particular the grids which involve $H\beta_G$ where the Thomas models appear to overpredict the value of the index. In many cases, points from both the high- and low-redshift sample lie off the model grids. Because of this, the absolute luminosity-weighted mean age of a particular galaxy returned may be improbably old. We therefore concentrate on the median relative difference in luminosity-weighted mean age, metallicity and $[\alpha/Fe]$ between the samples and use these, rather than absolute values of the physical properties, to interpret our results.

We fit the three indices simultaneously, and linearly interpolate between points on the model grid. We also extrapolate linearly beyond the edge of the grid. The values of age, $[M/H]$ and $[\alpha/Fe]$ which minimise χ^2 in $H\beta_G$, Mgb and $\langle Fe \rangle$ are adopted. Errors are estimated by doing the same at the 6 extreme points of the error ellipsoid defined by the uncertainties on the indices. Half the maximum of the differences at these 6 points is used at the uncertainty estimate. This representation of the uncertainty is consistent with the results of Monte-Carlo simulations of the model inversion. In these simulations, we use a subset of galaxies in the low-redshift sample, and vary the errors in $H\beta_G$, Mgb and $\langle Fe \rangle$ with Poissonian probability. The standard deviation of values in luminosity-weighted mean age, $[M/H]$, and $[\alpha/Fe]$ more closely match the errors derived using the maximum differences than the mean or median differences of the points in the error ellipsoid.

The results are shown in Figure 8. Correlations between age, $[M/H]$ and velocity dispersion, and $[\alpha/Fe]$ and velocity dispersion (Jørgensen 1999; Trager et al. 2000) are documented for galaxies at low redshift. We quantify the $\{\log \text{age}, [M/H], \log \sigma\}$ plane by extending the method used to fit our scaling relations to three dimensions. An equation of the form,

$$\log \text{age} = (-1.51 \pm 0.01)[M/H] + (1.79 \pm 0.23) \log \sigma - (2.75 \pm 0.02)$$

is fit to the low-redshift data by minimising absolute residuals perpendicular to the plane. This plane is

⁵ $[MgFe]' = \sqrt{Mgb \cdot (0.72 \text{ Fe5270} + 0.28 \text{ Fe5335})}$

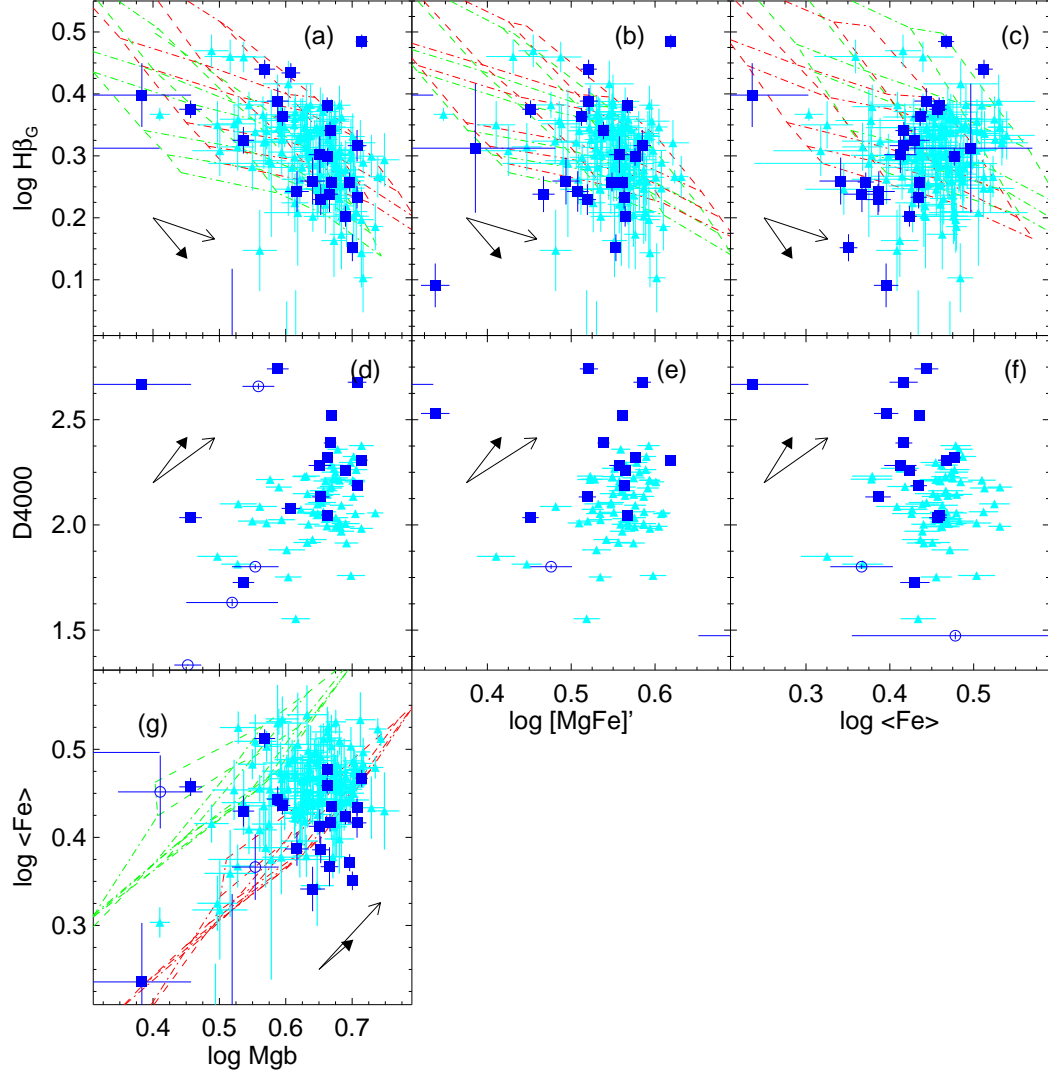


FIG. 7.— Visible line indices and D4000 versus each other. The plotting symbols are the same as those in Figure 5. Where available, we also overlay the grids of Thomas et al. (2003a, 2004), color-coded by $[\alpha/\text{Fe}]$ ratio. Green represents $[\alpha/\text{Fe}] = 0.0$ and red $[\alpha/\text{Fe}] = 0.3$. Dashed lines are lines of constant metallicity with values of $[\text{M}/\text{H}] = -0.30, 0.00, 0.35, 0.67$. The dot-dashed lines indicate metallicity changes at constant age with 1, 2, 4, 8, 11 and 15 Gyr. The arrows show the approximate changes in the indices for a change of $\Delta \log \text{age} = 0.3$ (solid arrow) and $\Delta [\text{M}/\text{H}] = 0.3$ (open arrow). The ordinate axis in panels (b) and (e) is designed such that quantities are independent of $[\alpha/\text{Fe}]$.

broadly consistent with that of Jørgensen (1999) and Trager et al. (2000) (see Figure 8). As with our previous fits for RXJ0142.0+2131 data points, we preserve the slope of this relation and find a median offset of 0.14 ± 0.07 in log age. This means that at a given velocity dispersion and metallicity, the luminosity-weighted mean ages of galaxies in RXJ0142.0+2131 are 0.14 ± 0.07 dex *older* than they are in the low-redshift sample. We address the somewhat counter-intuitive notion that galaxies at higher redshift can have older stellar populations than those in the local universe in §5. We also fit the scaling relation in $[\alpha/\text{Fe}]$ vs. $\log \sigma$, using the method outlined in §4.3. The galaxies in RXJ0142.0+2131 have a me-

dian value of $[\alpha/\text{Fe}]$ which is 0.14 ± 0.03 higher than the comparison sample.

Figure 8 shows these relationships, using a representative value of $\log \sigma = 2.2$ in the age-metallicity diagram. It also shows a side-on view of the $\{\log \text{age}, [\text{M}/\text{H}], \log \sigma\}$ plane in Figure 8d. In this view it appears evident that there is a bimodality in the luminosity-weighted mean ages of galaxies in RXJ0142.0+2131. There is no spatial clustering or coincidence of redshifts for galaxies with $\log \text{age} > 1.0$, although they do include 5 of the 6 brightest galaxies in the spectroscopic sample. The six galaxies in RXJ0142.0+2131 which appear to lie on the $\log \sigma - [\alpha/\text{Fe}]$ relation found at low redshift (those with $0.05 < [\alpha/\text{Fe}]$

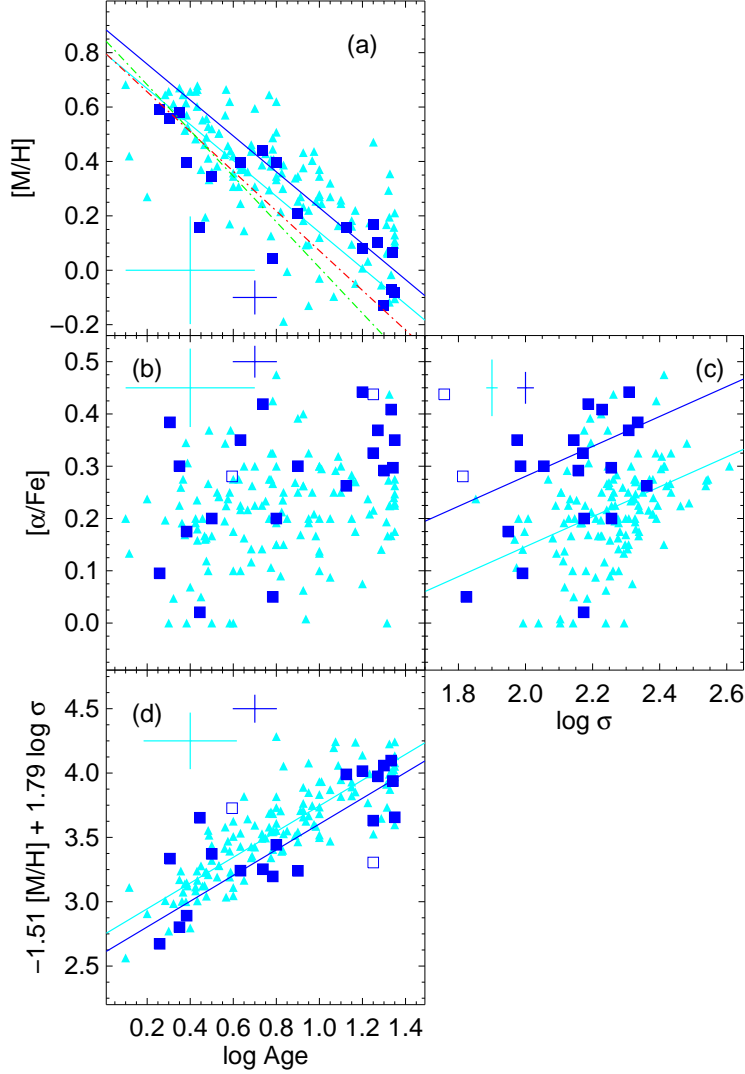


FIG. 8.— Derived relative physical attributes of cluster galaxies plotted against each other. Triangles are galaxies in the local sample, while squares are non-emission line galaxies in RXJ0142.0+2131, open symbols denoting galaxies excluded from the fits described in the text. The error bars show the median error in each sample. The fits to the points are shown as solid lines. In (a) the lines represent the age-metallicity relationship for galaxies with $\log \sigma = 2.2$ in each sample; relations found by Jørgensen (1999) and Trager et al. (2000) are denoted by the dot-dashed lines, green and red respectively. Panel (d) shows edge-on view of the $\log \text{age} - [\text{M}/\text{H}] - \log \sigma$ plane.

< 0.28) display no obvious spatial clustering.

5. DISCUSSION

In this section we first assess the derived offsets in our scaling relations and their consequences for the passive evolution model. We then discuss the evidence for stellar populations with older luminosity-weighted mean ages and larger $[\alpha/\text{Fe}]$ ratios in RXJ0142.0+2131. Finally we speculate on scenarios which can give rise to the inferred properties of galaxies in RXJ0142.0+2131, and the evolution of such a cluster to $z \sim 0$.

Of the scaling relations involving age indicators, the Faber-Jackson relation is consistent with passive evolution while the Balmer line indices are inconsistent only at the 1σ level. D4000 gives a much stronger result: its val-

ues are inconsistent with passive evolution at > 4 times the uncertainty. D4000 has been invoked as an age indicator (e.g. Tremonti et al. 2001; Kauffmann et al. 2003), though metallicity is at least as significant according to the relation given in Table 4.

The scaling relations for Mgb, CN_2 , CaHK, CN3883, G4300 in RXJ0142.0+2131 are offset in the direction opposite to that predicted by passive evolution. When combined, this offset is 5 times the uncertainty. $\langle \text{Fe} \rangle$ and C4668 are the only metal indices that are consistent with the passive-evolution model.

For the pure passive evolution scenario to be correct, either our data or the SSP models have to be wrong. Systematic errors in the velocity dispersion have already

been taken into account when arriving at the above results. We consider systematics affecting the line indices unlikely: the only scaling relations consistent with passive evolution belong to those indices whose dependence on age is small relative to that on metallicity or $[\alpha/\text{Fe}]$. Furthermore, the scaling relations with significant offset all indicate older ages. It is difficult to imagine a systematic error that could produce such a consistent offset, as some indices would have to get stronger and some weaker.

SSPs with non-solar $[\alpha/\text{Fe}]$ are yet to be widely tested or used. Nevertheless their age dependencies are generally consistent with those that employ solar $[\alpha/\text{Fe}]$ (e.g. Vazdekis et al. 1997). We note that none of the results presented in §4.3 are changed if we use the model line indices in Vazdekis et al. (1997) as our reference, as opposed to those of Thomas et al. The inconsistency of the results with the passive evolution model is thus not a consequence of our comparison with the Thomas models.

The assertion that the $[\alpha/\text{Fe}]$ ratio in members of RXJ0142.0+2131 is enhanced over the control sample makes use of the indices' dependence on $[\alpha/\text{Fe}]$ specific to the Thomas models. Even so, it is generally accepted that Mgb is more sensitive to Mg than to Fe, and $\langle\text{Fe}\rangle$ is more sensitive to iron than to α elements. The relative strength of Mgb in Figure 6a and weakness of $\langle\text{Fe}\rangle$ in Figure 6b, combined with the high ratio of the the Mgb index to $\langle\text{Fe}\rangle$ in Figure 7g, indicates directly that $[\alpha/\text{Fe}]$ is enhanced in RXJ0142.0+2131. Even if $[\alpha/\text{Fe}]$ is not yet accurately modeled, we are forced to conclude, albeit in a qualitative sense, that it is significantly enhanced compared with the low-redshift sample.

By inverting the models for $\text{H}\beta_{\text{G}}$, Mgb , and $\langle\text{Fe}\rangle$, we calculate that, at a given velocity dispersion and metallicity, galaxies in RXJ0142.0+2131 have luminosity-weighted mean ages 0.14 ± 0.07 dex older than the comparison sample. A similar analysis indicates that $[\alpha/\text{Fe}]$ in stellar populations in RXJ0142.0+2131 is 0.14 ± 0.03 greater than at low redshift.

Three indices are used to obtain these offsets. In order to give preference to this interpretation over the pure passive evolution model, we must test these values against all scaling relations, and in particular those which show consistency with passive evolution. We find that the offsets for all indices in Table 4 modeled by Thomas are consistent with $\Delta \log \text{age} = 0.14$ and $\Delta[\alpha/\text{Fe}] = 0.14$. This check is more difficult to make for the CMD, the FJ relation, D4000, CaHK, and CN3883 for which the models assume solar abundance ratios. In these instances we gauge whether the $[\alpha/\text{Fe}]$ dependence required, given the difference in log age and the equations in Table 4, is feasible. CN3883 requires only a weak correlation with $[\alpha/\text{Fe}]$, similar to the related index CN2. If we assume that the dependence is the same, then CN3883 is consistent with our derived offsets.

Only about half of the average difference in the 4000Å break can be explained by $\Delta \log \text{age} = 0.14$. In order to be consistent with our $[\alpha/\text{Fe}]$ offset, D4000 would have to become stronger with increasing α -element abundance ratio. For our low-redshift sample, we find that D4000 is weakly positively correlated with $[\alpha/\text{Fe}]$. J05 also found evidence for such a correlation. The greater average strength of the 4000Å break therefore appears qualitatively consistent with our estimated offsets in age and abundance ratio.

A greater problem is presented by the FJ relation and the CMD. Stellar populations with $\Delta \log \text{age} = 0.14$ are expected to be ~ 0.3 mag fainter than the comparison sample. For our FJ relation to be consistent with our derived offsets, the B -band mass-to-light ratio of a galaxy would have to decrease with increasing α -element abundance ratio. Furthermore, for the CMD to remain consistent, either the observed r' -band magnitude would have to brighten, or stellar populations would have to become bluer, with increasing $[\alpha/\text{Fe}]$. There are no models which predict the behavior of magnitude and color vs. $[\alpha/\text{Fe}]$. However, Thomas & Maraston (2003) indicate that blue luminosity increases with increasing $[\alpha/\text{Fe}]$, which would work to push older stellar populations in the CMD and FJ relations back toward consistency with the passive evolution predictions. As far as the CaHK index is concerned, we require that it becomes stronger with increasing $[\alpha/\text{Fe}]$. This seems sensible, given that Ca is itself an α -element. However, Ca has been found to be under-abundant compared with other α -elements in local early-type galaxies (Thomas et al. 2003b). There are also no SSP models which estimate its dependence on $[\alpha/\text{Fe}]$. Because of this rather complex relationship, we note that the CaHK index is incompatible with the passive evolution model but can provide no evidence to support our alternative model.

The scaling relations for indices modeled with $[\alpha/\text{Fe}]$ are consistent with $\Delta \log \text{age} = 0.14$ and $\Delta[\alpha/\text{Fe}] = 0.14$. Furthermore, those scaling relations (including the CMD and the FJ relation) involving observables whose dependence on $[\alpha/\text{Fe}]$ is not known display, qualitatively, the behavior expected of older stellar populations with enhanced abundance ratios. We conclude that the combined scaling relations show that galaxies in RXJ0142.0+2131 have greater $[\alpha/\text{Fe}]$ than those at $z \sim 0$ and cannot evolve into them by passive evolution.

Two questions immediately arise from stellar populations in RXJ0142.0+2131 with higher $[\alpha/\text{Fe}]$ than those in low-redshift clusters. Firstly, how do cluster galaxies come to have high $[\alpha/\text{Fe}]$ ratios? Secondly, is there a mechanism by which stellar populations in RXJ0142.0+2131 can reduce their $[\alpha/\text{Fe}]$ and become like those at $z \sim 0$?

Enhanced $[\alpha/\text{Fe}]$ ratios can be produced by a short episode of star formation which is curtailed before the lower-mass stars can produce significant Fe-peak elements through Type I supernovae. In a scenario such as this the luminosity-weighted mean ages of galaxies would be higher than expected because ongoing star-formation is absent. Such an episode would have to be quenched within ~ 1 Gyr to prevent the products of Type Ia SNe contaminating a subsequent generation of stars. This can be mitigated to some extent if the star formation episode is violent enough to produce a top-heavy IMF which will give a higher yield of α elements per unit luminosity (e.g. see Worthey et al. 1992).

If RXJ0142.0+2131 formed rapidly in a cluster merger, the stripping of gas from galaxies in such an event could be used to explain the rapid quenching of star-formation. The large velocity dispersion of RXJ0142.0+2131 might thereafter inhibit the merging of cluster members and the associated decrease of $[\alpha/\text{Fe}]$ and luminosity-weighted mean age. This could also be used to explain the lack of a dominant galaxy. It does not, however, explain the

rather ordinary fraction of blue galaxies, which we might expect to be higher than normal because of the absence of merging. Values of $[\alpha/\text{Fe}]$ for stellar populations have yet to be estimated in a large number of distant clusters, so it is unclear whether RXJ0142.0+2131 is unusual in this respect. However, the difference in the implied luminosity-weighted mean ages does mean that any evolution from the stellar populations in RXJ0142.0+2131 to those in our comparison sample cannot be by pure passive evolution.

No substructure is detectable in RXJ0142.0+2131 based on our data, and there is no evidence for an excess of star-forming, or post-starburst galaxies. However, its position on the $B_{gc} - \log \sigma$ and $L_X - \log \sigma$ suggests a large cluster velocity dispersion for its luminous mass. In terms of its position on the B_{gc} vs. $\log \sigma$ plot, RXJ0142.0+2131 most resembles MS 1455+22 at $z = 0.26$, (see Yee & Ellingson 2003). However, MS 1455+22 has a very large cD galaxy, strong cooling flow, and a very low fraction of blue galaxies. In local terms, the cluster closest to RXJ0142.0+2131 in $B_{gc} - \log \sigma$ is Abell 85 at $z = 0.055$ (Yee & López-Cruz 1999). Abell 85 is in the early stages of a merger and has a moderately strong cooling flow associated with a cD galaxy (Kempner et al. 2002; Durret et al. 2003). It seems unlikely, therefore, that there is much correspondence between RXJ0142.0+2131 and either of these clusters. It is possible that RXJ0142.0+2131 has no analogy in the low-redshift universe, or that local surveys cannot discover massive, underluminous clusters. This seems highly improbable as such clusters should still be detectable to X-ray observatories. RXJ0142.0+2131 could have a significantly lower X-ray luminosity than inferred from the ROSAT observation if there is a contribution to the X-ray flux from obscured AGNs which ROSAT cannot resolve spatially. *Chandra* or *XMM-Newton* observations would be invaluable in resolving this question. However, the problem of the prodigious cluster velocity dispersion remains whether or not there is significant X-ray flux in AGNs. There remain hints that the centre of RXJ0142.0+2131 is not yet fully virialized; for example, the lack of a dominant galaxy, the velocity offset of the brightest member from the cluster centre and the distance between the brightest and second brightest members. It is clear that RXJ0142.0+2131 is an unusual cluster of galaxies. Further study, and in particular high-resolution X-ray observations, will be invaluable in discerning its nature.

Whatever its history, it is difficult, if not impossible, to imagine a scenario by which the galaxies in RXJ0142.0+2131 can evolve, in the ~ 3 Gyr available, from their state at $z = 0.28$ to that of our comparison sample. Star formation (which is not present at $z = 0.28$) would have to occur within the early-type population to decrease their luminosity-weighted mean ages. This would have to occur gradually in order to avoid enhancing the $[\alpha/\text{Fe}]$ even further, which presumably rules out a cluster merger event. Luminosity-weighted mean ages and abundance ratios could be reduced if there is a great deal of merging between elliptical and disk galaxies. However, the lack of an excess of blue galaxies and a high cluster velocity dispersion argues against an unusual amount of merging being able to take place. Furthermore, it has been argued that the blue

fraction is reduced mainly by the ageing of stellar populations (Balogh et al. 1999). It remains difficult to devise a mechanism in clusters by which a lot of merging, but little star formation, takes place.

6. CONCLUSIONS

We present GMOS-N broad-band and MOS observations of RXJ0142.0+2131, an X-ray luminous cluster of galaxies at $z = 0.28$. Redshifts, central velocity dispersions, and absorption-line indices for 43 objects are derived. Of the spectroscopic sample, 30 galaxies are members of RXJ0142.0+2131. We calculate the cluster velocity dispersion as $1278 \pm 134 \text{ km s}^{-1}$ and find no sign of substructure. Our broad-band observations show RXJ0142.0+2131 to be a poor cluster with a blue fraction consistent with other clusters at $z \sim 0.3$. It appears to have a very large velocity dispersion for both its richness and X-ray luminosity.

The $(g' - r')$ vs. r' red sequence for RXJ0142.0+2131 is consistent with a passively evolving population of early-type galaxies formed at $z_{\text{form}} \simeq 2$.

We have established scaling relations between the absolute B -band magnitude and central velocity dispersion (the Faber-Jackson relation), as well as relations between absorption line indices and central velocity dispersion for galaxies in RXJ0142.0+2131. These are compared with the low-redshift sample and predictions from single stellar population models. The Faber-Jackson relation is in agreement with a pure passive evolution model and the Balmer indices ($H\beta_G$, $H\delta_A + H\gamma_A$) are in marginal disagreement. The scaling relations for Mgb , CN_2 , CaHK , $\text{CN}3883$, and G4300 indices, when taken together, are offset from the pure passive evolution model with five times the uncertainty.

We use the models of Thomas et al. and the measured indices $\{H\beta_G, \text{Mgb}, \langle \text{Fe} \rangle\}$ to compute the relative differences in luminosity-weighted mean age, metallicity and α -element abundance ratio between stellar populations in RXJ0142.0+2131 and the low-redshift comparison sample. We find that for a particular metallicity and velocity dispersion, RXJ0142.0+2131 has stellar populations with luminosity-weighted $\log \text{age} = 0.14 \pm 0.07$ older than our comparison sample. We also show that galaxies in RXJ0142.0+2131 have $[\alpha/\text{Fe}]$ 0.14 ± 0.03 greater than the local cluster galaxies. All scaling relations are consistent with these values, and so we consider this scenario more likely than one in which stellar populations evolve passively. We speculate that these enhancements were caused by rapid bursts of star formation that were subsequently curtailed.

RXJ0142.0+2131 appears to be without a counterpart in the local universe. Current models of cluster evolution are unable to provide a path by which RXJ0142.0+2131 can evolve into our low-redshift comparison sample. We believe that the morphology of the cluster gas in RXJ0142.0+2131 will provide clues as to its formation history. X-ray observations with high spatial resolution will be required for this analysis.

The GMOS instrument, commissioning and System Verification teams are thanked for their effort in making GMOS an efficient Gemini facility instrument. The observations used in this paper were obtained

as part of the System Verification observations, program ID GN-2001B-SV-51. RLD is grateful for the award of a PPARC Senior Fellowship (grant number PPA/Y/S/1999/00854). Based on observations obtained at the Gemini Observatory, which is operated by the Association of Universities for Research in Astronomy, Inc., under a cooperative agreement with the NSF on behalf

of the Gemini partnership: the National Science Foundation (United States), the Particle Physics and Astronomy Research Council (United Kingdom), the National Research Council (Canada), CONICYT (Chile), the Australian Research Council (Australia), CNPq (Brazil) and CONICET (Argentina).

REFERENCES

- Aaronson, M., Bothun, G., Mould, J., Huchra, J., Schommer, R. A., & Cornell, M. E. 1986, *ApJ*, 302, 536
- Andreon, S., Willis, J., Quintana, H., Valtchanov, I., Pierre, M., & Pacaud, F. 2004, *MNRAS*, 353, 353
- Balogh, M. L., Morris, S. L., Yee, H. K. C., Carlberg, R. G., & Ellingson, E. 1999, *ApJ*, 527, 54
- Beers, T. C., Flynn, K., & Gebhardt, K. 1990, *AJ*, 100, 32
- Bell, E. F., et al. 2004, *ApJ*, 608, 752
- Bender, R., Burstein, D., & Faber, S. M. 1993, *ApJ*, 411, 153
- Bender, R., Saglia, R. P., Ziegler, B., Belloni, P., Greggio, L., Hopp, U., & Bruzual, G. 1998, *ApJ*, 493, 529
- Bertin, E. & Arnouts, S. 1996, *AASS*, 117, 393
- Böhringer, H. et al. 2000, *ApJS*, 129, 435
- Bower, R. G., Lucey, J. R., & Ellis, R. S. 1992, *MNRAS*, 254, 601
- Bruzual A., G. 1983, *ApJ*, 273, 105
- Bruzual, G. & Charlot, S. 2003, *MNRAS*, 344, 1000
- Butcher, H. & Oemler, A. 1984, *ApJ*, 285, 426
- Cardelli, J. A., Clayton, G. C., & Mathis, J. S. 1989, *ApJ*, 345, 245
- Colless, M., Burstein, D., Davies, R. L., McMahan, R. K., Saglia, R. P., & Wegner, G. 1999, *MNRAS*, 303, 813
- Danese, L., de Zotti, G., & di Tullio, G. 1980, *A&A*, 82, 322
- Davidge, T. J. & Clark, C. C. 1994, *AJ*, 107, 946
- Davies, R. L., Sadler, E. M., & Peletier, R. F. 1993, *MNRAS*, 262, 650
- Djorgovski, S. & Davis, M. 1987, *ApJ*, 313, 59
- Donahue, M., Daly, R. A., & Horner, D. J. 2003, *ApJ*, 584, 643
- Dressler, A. 1980, *ApJ*, 236, 351
- Dressler, A., Lynden-Bell, D., Burstein, D., Davies, R. L., Faber, S. M., Terlevich, R., & Wegner, G. 1987, *ApJ*, 313, 42
- Dressler, A. & Shectman, S. A. 1988, *AJ*, 95, 985
- Dressler, A., et al. 1997, *ApJ*, 490, 577
- Durret, F., Lima Neto, G. B., Forman, W., & Churazov, E. 2003, *A&A*, 403, L29
- Ebeling, H., Edge, A. C., Allen, S. W., Crawford, C. S., Fabian, A. C., & Huchra, J. P. 2000, *MNRAS*, 318, 333
- Faber, S. M. & Jackson, R. E. 1976, *ApJ*, 204, 668
- Fabian, A. C., et al. 2000, *MNRAS*, 318, L65
- Fairley, B. W., Jones, L. R., Wake, D. A., Collins, C. A., Burke, D. J., Nichol, R. C., & Romer, A. K. 2002, *MNRAS*, 330, 755
- Gebhardt, K. et al. 2000, *AJ*, 119, 1157
- Gebhardt, K., et al. 2003, *ApJ*, 597, 239
- Gladders, M. D., Lopez-Cruz, O., Yee, H. K. C., & Kodama, T. 1998, *ApJ*, 501, 571
- González, J. J. 1993, PhD Thesis, Univ. California, Santa Cruz
- Gorgas, J., Cardiel, N., Pedraz, S., & González, J. J. 1999, *A&AS*, 139, 29
- Hook, I. M., Jørgensen, I., Allington-Smith, J. R., Davies, R. L., Metcalfe, N., Murowinski, R. G., & Crampton, D. 2004, *PASP*, 116, 425
- Jørgensen, I., Franx, M., & Kjaergaard, P. 1995, *MNRAS*, 273, 1097
- Jørgensen, I., Franx, M., & Kjaergaard, P. 1996, *MNRAS*, 280, 167
- Jørgensen, I. 1997, *MNRAS*, 288, 161
- Jørgensen, I. 1999, *MNRAS*, 306, 607
- Jørgensen, I., Bergmann, M., Davies, R. L., Barr, J. M., Takamiya, M., Crampton, D. 2005, *AJ*, 129, 1249 (J05)
- Kauffmann, G., et al. 2003, *MNRAS*, 341, 33
- Kelson, D. D., Illingworth, G. D., van Dokkum, P. G., & Franx, M. 2000, *ApJ*, 531, 184
- Kelson, D. D., Illingworth, G. D., Franx, M., & van Dokkum, P. G. 2001, *ApJ*, 552, L17
- Kempner, J. C., Sarazin, C. L., & Ricker, P. M. 2002, *ApJ*, 579, 236
- Kodama, T. & Arimoto, N. 1997, *A&A*, 320, 41
- Kuntschner, H. 2000, *MNRAS*, 315, 184
- Longair, M. S. & Seldner, M. 1979, *MNRAS*, 189, 433
- Mahdavi, A. & Geller, M. J. 2001, *ApJ*, 554, L129
- Maraston, C. 2004, *MNRAS*, submitted (astro-ph/0410207)
- Merritt, D. 1997, *AJ*, 114, 228
- Owen, F. N., Ledlow, M. J., Keel, W. C., Wang, Q. D., & Morrison, G. E. 2005, *AJ*, 129, 31
- Peng, C. Y., Ho, L. C., Impey, C. D., & Rix, H. 2002, *AJ*, 124, 266
- Postman, M., Lauer, T. R., Szapudi, I., & Oegerle, W. 1998, *ApJ*, 506, 33
- Saha, P. & Williams, T. B. 1994, *AJ*, 107, 1295
- Sakai, S., Kennicutt, R. C., van der Hulst, J. M., & Moss, C. 2002, *ApJ*, 578, 842
- Schlegel, D. J., Finkbeiner, D. P., & Davis, M. 1998, *ApJ*, 500, 525
- Seldner, M. & Peebles, P. J. E. 1978, *ApJ*, 225, 7
- Sérsic, J. L. 1968, *Atlas de Galaxies Australes*; Vol. Book; Page 1, 0
- Smail, I., Edge, A. C., Ellis, R. S., & Blandford, R. D. 1998, *MNRAS*, 293, 124
- Smith, J. A., et al. 2002, *AJ*, 123, 2121
- Thomas, D., & Maraston, C. 2003, *A&A*, 401, 429
- Thomas, D., Maraston, C., & Bender, R. 2003a, *MNRAS*, 339, 897
- Thomas, D., Maraston, C., & Bender, R. 2003b, *MNRAS*, 343, 279
- Thomas, D., Maraston, C., & Korn, A. 2004, *MNRAS*, 351, L19
- Trager, S. C., Faber, S. M., Worthey, G., & González, J. J. 2000, *AJ*, 120, 165
- Tremonti, C. A., Heckman, T. M., Kauffmann, G., & Charlot, S. 2001, *Bulletin of the American Astronomical Society*, 33, 1422
- van Dokkum, P. G. & Franx, M. 1996, *MNRAS*, 281, 985
- van Dokkum, P. G., Franx, M., Kelson, D. D., & Illingworth, G. D. 2001, *ApJ*, 553, L39
- Vazdekis, A., Peletier, R. F., Beckman, J. E., & Casuso, E. 1997, *ApJS*, 111, 203
- Voges, W. et al. 1999, *A&A*, 349, 389
- Wilson, G. 2003, *ApJ*, 585, 191
- Wold, M., Lacy, M., Lilje, P. B., & Serjeant, S. 2000, *MNRAS*, 316, 267
- Worthey, G., Faber, S. M., & Gonzalez, J. J. 1992, *ApJ*, 398, 69
- Worthey, G., Faber, S. M., Gonzalez, J. J., & Burstein, D. 1994, *ApJS*, 94, 687
- Worthey, G. & Ottaviani, D. L. 1997, *ApJS*, 111, 377
- Wuyts, S., van Dokkum, P. G., Kelson, D. D., Franx, M., & Illingworth, G. D. 2004, *ApJ*, 605, 677
- Yee, H. K. C. & López-Cruz, O. 1999, *AJ*, 117, 1985
- Yee, H. K. C. & Ellingson, E. 2003, *ApJ*, 585, 215
- Zabludoff, A. I., Huchra, J. P., & Geller, M. J. 1990, *ApJS*, 74, 1
- Ziegler, B. L. & Bender, R. 1997, *MNRAS*, 291, 527
- Ziegler, B. L., Bower, R. G., Smail, I., Davies, R. L., & Lee, D. 2001, *MNRAS*, 325, 1571

APPENDIX

GMOS-N DATA REDUCTION

Imaging data

Broad-band images in g' , r' and i' are bias-subtracted and then flatfielded using twilight skyflats. Fringing is significant (at about 1% of the sky background) in the i' band, while scattered light needs to be removed from all

TABLE A6
PHOTOMETRIC ZERO POINTS AND COLOR TERMS FOR PHOTOMETRIC CALIBRATION

filter	m_{zero}	rms	Color term fit	Δm_{zero}	rms (fit)	Color interval
	(1)	(2)	(3)		(4)	(5)
g'	27.88 ± 0.01	0.044^{a}	$(0.066 \pm 0.002)(g' - r') - (0.037 \pm 0.002)$		0.034	$-0.55 \leq (g' - r') \leq 2.05$
r'	28.15 ± 0.01	0.045^{b}	$(0.042 \pm 0.004)(r' - i') - (0.011 \pm 0.002)$		0.043	$-0.35 \leq (r' - i') \leq 2.20$
i'	27.86 ± 0.01	0.054^{b}	$(0.063 \pm 0.005)(r' - i') - (0.013 \pm 0.002)$		0.050	$-0.35 \leq (r' - i') \leq 2.20$

NOTE. — (1) Photometric zero point, (2) rms of Δm , equivalent to the expected uncertainty on the standard calibration if the color terms are ignored, (3) linear fits to the color terms, (4) rms of the linear fits, (5) color interval within which the linear fit applies.

^a $-1.10 \leq (g' - i') \leq 3.05$

^b $-0.7 \leq (r' - i') \leq 2.5$

frames. Scattered light and fringe frames are created by combining images in each filter with the brightest objects masked out. These are fitted with a smooth surface before being subtracted from each image. In the case of the i' -band, where fringing is significant, the fringe frame is median-smoothed with a $1''.8 \times 1''.8$ box before subtraction. Images are then registered and combined rejecting cosmic rays and bad pixels.

Photometric calibration

Flux calibrations are accomplished using observations of standard stars on UT 2001 October 21 under photometric conditions. Science exposures from other nights were normalised to the observations taken on UT 2001 October 21. The photometry is corrected for the effect of galactic extinction using the prescription of Cardelli et al. (1989) based on the measurement of $A_B = 0.292$ toward RXJ0142.0+2131 of Schlegel et al. (1998). Values of galactic extinction in each filter are $A_{g'} = 0.243$, $A_{r'} = 0.189$ and $A_{i'} = 0.150$.

Standard magnitudes are derived using the relation,

$$m_{\text{std}} = m_{\text{zero}} + \Delta m_{\text{zero}} - 2.5 \log(N/t) - k(\text{airmass} - 1)$$

where *airmass* is the mean airmass of the observation and k is the mean atmospheric extinction at Mauna Kea. Magnitude zero points and the dependence of Δm_{zero} on color are given in Table A6.

Our low-redshift comparison sample of galaxies is calibrated in rest-frame B . The exact transformation from $r'i'$ photometry to this system depends on the redshift. Full details of the methodology of rest-frame calibrations for clusters in the Gemini/HST Galaxy Cluster Project will be given in a future paper outlining the GMOS-N photometry for the project. The transformation from $r'i'$ to B_{rest} at the redshift of RXJ0142.0+2131 ($z = 0.280$) is,

$$B_{\text{rest}} = i' + 0.4753 + 1.6421(r' - i') - 0.0253(r' - i')^2$$

and in all cases, the absolute B -band magnitude is derived as

$$M_B = B_{\text{rest}} - DM(z) + 2.5 \log(1 + z)$$

where the distance modulus ($DM(z)$) for the cluster redshift in our adopted cosmology, is 40.78.

Spectroscopic data

Table A7 gives the positions, magnitudes and colors of galaxies in the spectroscopic sample.

Spectroscopic reductions are achieved using the Gemini IRAF package v1.4. The method follows J05 apart from two major differences, namely the inclusion of tilted slits and the lack of detectable fringing. Tilted slits (i.e. slits not perpendicular to the dispersion direction) were included, aligned along the major axes of the galaxies, for determination of galactic rotation curves. An analysis of this aspect of the data, as well as a determination of a Tully-Fisher relation for RXJ0142.0+2131 will be presented in a future paper. At the present time we merely outline the extra steps in the reduction process which result from this intricacy.

Bias-subtraction and overscan-trim are carried out in standard fashion using the same method as the imaging data. Flatfields are created from lamp spectra and applied on a chip-by-chip basis.

To subtract the sky, which includes strong emission lines, we use a technique which avoids the interpolation of the data which occurs during wavelength calibration. A second-order Chebyshev polynomial is fit in the spatial direction column by column, rejecting points $\pm 3\sigma$ above and below the fit and an object-centred aperture of between $1''.4$ and $6''.1$ depending on the spatial extent of the object. This sky is then subtracted.

For objects observed through tilted slits the spectra must be rectified in order to fit the sky. The angle of the slit on the mask and the angle of lines in the dispersed spectrum differ by the anamorphic factor, which is a function of grating angle and slit position. As a consequence, we use between 3 and 5 strong skylines in each spectrum to determine the best rectification angle on a spectrum-by-spectrum basis. This is typically between 80% and 90% of the

TABLE A7
PHOTOMETRIC PROPERTIES OF THE SPECTROSCOPIC SAMPLE

ID	RA (J2000)	Dec (J2000)	g'	r'	i'	$(g' - r')$	$(g' - i')$	B/D
1	1:42:09.11	21:33:23.8	19.20	18.02	17.50	1.57	2.17	B
22	1:42:08.68	21:33:22.6	20.03	18.97	18.47	1.62	2.22	B
44	1:42:10.37	21:33:32.2	22.62	21.36	20.87	1.32	1.85	...
88	1:42:09.21	21:33:14.0	18.48	19.59	19.40	1.14	1.57	D
116	1:41:54.76	21:33:08.5	21.00	20.19	19.85	0.92	1.35	D
128	1:42:07.37	21:33:02.1	20.79	19.38	18.88	1.50	2.08	B
173	1:41:56.30	21:32:54.9	21.08	20.20	19.80	1.02	1.50	...
205	1:42:04.40	21:32:39.8	20.10	18.89	18.45	1.42	1.97	B
241	1:41:55.86	21:32:39.8	20.60	19.66	19.26	0.92	1.36	...
318	1:41:57.29	21:32:27.8	21.19	20.35	19.93	0.85	1.32	D
322	1:42:03.69	21:32:15.3	20.72	19.30	18.74	1.49	2.07	B
379	1:42:01.92	21:32:10.2	20.80	19.28	18.70	1.60	2.20	B
412	1:42:02.45	21:31:57.6	19.88	18.64	18.09	1.63	2.24	B
442	1:42:02.64	21:32:06.5	22.63	21.26	20.77	1.43	1.95	B
450	1:42:02.94	21:31:04.1	17.66	17.24	16.97	0.49	0.80	...
451	1:42:01.13	21:31:55.1	20.62	19.18	18.63	1.85	2.54	...
479	1:42:03.46	21:31:17.4	18.25	17.20	16.71	1.58	2.18	B
490	1:42:00.43	21:31:44.7	18.97	17.66	17.06	1.38	2.00	...
537	1:42:08.64	21:31:45.5	21.75	20.42	19.86	1.44	2.04	B
614	1:42:01.26	21:31:32.0	21.70	20.21	19.67	1.56	2.14	B
637	1:42:01.38	21:31:22.1	21.39	19.88	19.38	1.56	2.15	B
671	1:42:03.21	21:31:11.9	19.71	18.29	17.72	1.66	2.29	B
760	1:42:01.28	21:31:04.6	21.90	20.41	19.86	1.56	2.15	B
777	1:41:59.76	21:30:57.9	21.17	19.64	19.05	1.65	2.28	B
844	1:42:07.17	21:30:49.7	21.54	20.14	19.62	1.49	2.07	B
900	1:42:09.16	21:30:40.6	21.38	20.78	20.58	0.78	1.11	D
911	1:42:03.11	21:30:31.6	22.51	21.12	20.58	1.43	1.99	B
971	1:42:06.33	21:30:24.9	21.50	20.86	20.52	0.70	1.07	...
1012	1:42:01.75	21:30:17.4	22.24	20.73	20.18	1.53	2.11	B
1029	1:41:55.20	21:30:12.1	21.70	20.31	19.76	1.47	2.05	B
1043	1:41:58.57	21:30:01.9	20.70	19.28	18.74	1.52	2.11	B
1076	1:42:05.61	21:30:01.3	21.94	20.96	20.44	1.57	2.26	...
1099	1:42:05.63	21:30:03.4	22.16	21.36	21.03	0.91	1.27	D
1154	1:41:54.38	21:29:51.1	21.27	20.38	20.09	0.95	1.32	...
1179	1:42:00.91	21:29:41.6	20.89	19.85	19.37	1.16	1.76	D
1205	1:41:53.41	21:29:26.7	21.29	19.87	19.35	1.49	2.08	D
1207	1:42:04.04	21:29:35.5	21.85	20.40	19.82	1.52	2.13	B
1242	1:42:06.39	21:29:27.0	22.39	21.18	20.45	1.35	2.18	...
1325	1:41:57.25	21:28:27.9	21.66	19.96	19.32	1.83	2.51	...
1412	1:42:07.28	21:28:56.5	21.30	20.22	19.78	1.44	2.01	D
1416	1:42:06.40	21:28:38.7	21.49	20.33	19.82	1.31	2.00	D
1461	1:42:08.24	21:29:12.1	21.06	20.71	20.58	0.41	0.60	...
1472	1:42:08.28	21:28:49.0	21.98	20.98	20.35	1.11	2.00	...

NOTE. — Units of right ascension are hours, minutes, and seconds, and units of declination are degrees, arcminutes, and arcseconds. Right ascension and declination are consistent with USNO, with an rms scatter of $\approx 0''.7$. Magnitudes and colors are corrected for galactic extinction. B/D gives an estimate (for cluster members) of whether the r' -band morphology is bulge-like or disk-like (see text).

tilt in the slit mask. Spectra are straightened by shifting individual rows in multiples of a fifth of a pixel. The sky is then subtracted as described above, and the spectra are restored to their original orientation.

Subtracted sky spectra are retained and processed in the same way as the science from this point.

The sky-subtracted exposures taken at the same central wavelength setting are combined. Bad pixels and cosmic rays are rejected at this stage. Then the images are mosaicked using the correct transformation for the relative position of the GMOS-N CCDs. The spectra are wavelength-calibrated using CuAr spectra taken using the same instrumental setup as the science observations. Calibrated spectra at each central wavelength setting are co-added and those objects which appear in both masks are also combined.

The 2D spectra are traced and extracted as 1D spectra using an aperture of $1''.2$ centred on the maximum signal perpendicular to the spectrum. Atmospheric telluric absorption lines are corrected for by combining all spectra into a single spectrum. A 27-piece cubic spline fit is used to normalise the resulting spectrum with pixels $\pm 3\sigma$ from the fit rejected. Regions unaffected by telluric lines are set to unity. Figure A9 shows the combined spectrum and the function used for telluric correction.

The instrumental resolution for each slit ranges from $1.4 - 1.6\text{\AA}$, measured from Gaussian fits to the sky lines. Spectra are resampled to 0.92\AA per pixel to improve signal-to-noise. A relative flux calibration is then achieved using a sensitivity function covering the full spectral range of the MOS spectra (see J05 for details).

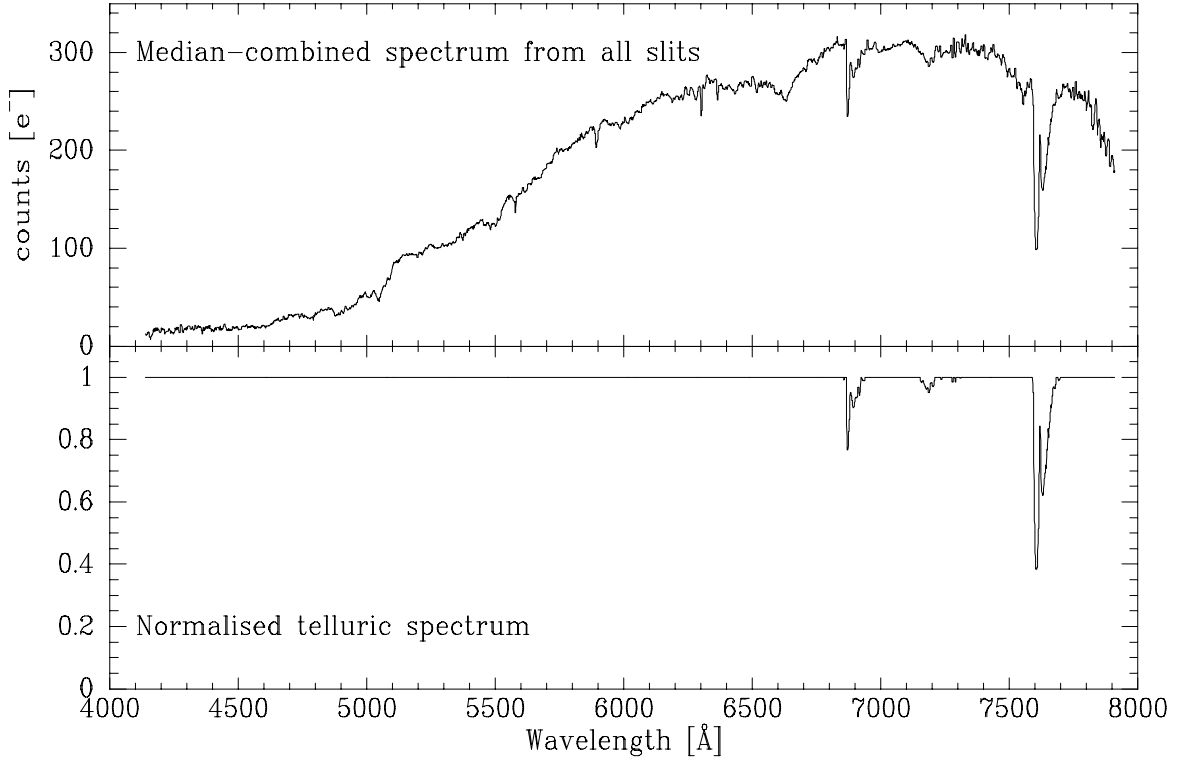


FIG. A9.— *Top*: Spectrum formed from median-combining spectra of all objects. *Bottom*: Normalised telluric absorption spectrum.

GMOS-N SPECTROSCOPIC RESULTS

Derived redshifts, velocity dispersions and stellar template fractions for all galaxies are given in Table B8. Table B9 gives the line indices and corresponding uncertainties for the spectroscopic sample, excluding the M star.

Figure B10 show rest-frame object and noise spectra for the 30 cluster members in our spectroscopic sample together with their magnitudes, colors and velocity dispersions. Figure B11 is the corresponding figure for non-members. The spectrum of the M star is not shown.

Postage stamp images of the cluster members in the spectroscopic sample are presented in Figure B12. These are constructed from the GMOS-N g' , r' , and i' filters. The equivalent postage stamps for non-members are shown in Figure B13.

TABLE B9
LINE INDICES

ID	CN3883	CaHK	D4000	H δ_A	CN ₂	G4300	H γ_A	C4668	H β_G	Mgb	Fe5270	Fe5335	$\langle\text{Fe}\rangle$
1	-2.870	0.140	5.810	-5.660	8.300	1.810	4.970	2.730	1.970	2.351
1	0.159	0.005	0.120	0.238	0.131	0.062	0.073	0.074	0.075	0.053
22	...	20.790	...	-1.640	0.190	5.820	-6.180	4.340	1.420	5.020	2.940	1.550	2.242
22	...	0.404	...	0.217	0.006	0.154	0.323	0.152	0.069	0.077	0.077	0.078	0.055
44	0.070	-1.740	1.180	2.970	...	0.610	-3.770	3.490	-0.820	1.290
44	0.010	0.969	0.009	0.601	...	0.491	0.560	0.707	0.452	0.624
88	9.360	...	0.500	-1.810	5.800	2.050	1.660	4.100	2.170	3.137
88	0.911	...	0.665	1.474	1.194	0.492	0.682	0.702	0.797	0.531
116 ^{a,b}	...	11.790	1.630	-1.680	0.020	1.350	0.050	-5.600	0.730	3.310	0.240	...	0.222
116	...	1.468	0.017	1.061	0.027	0.808	0.877	1.093	0.427	0.493	0.550	...	0.506
128 ^a	...	19.980	...	-0.550	0.070	6.140	-4.710	6.080	1.730	4.630	2.530	...	2.326
128	...	0.531	...	0.295	0.009	0.228	0.523	0.243	0.113	0.129	0.129	...	0.118
173 ^b	0.120	13.880	1.830	3.520	0.020	2.400	-0.870	5.200	-0.290	1.810	2.770
173	0.010	0.585	0.007	0.338	0.010	0.539	0.304	0.313	0.201	0.171	0.208
205	0.220	20.880	2.030	-0.770	0.100	5.170	-4.020	5.070	2.370	2.860	2.700	3.030	2.866
205	0.006	0.328	0.004	0.197	0.006	0.150	0.180	0.175	0.077	0.103	0.100	0.094	0.069
241 ^b	0.090	9.530	1.410	3.410	...	0.950	2.720	2.360	0.530	2.240	2.070	1.900	1.982
241	0.006	0.415	0.004	0.263	...	0.223	0.235	0.282	0.129	0.153	0.152	0.145	0.105
318 ^b	0.040	9.450	1.330	3.320	...	2.430	-0.070	3.040	-4.790	2.830	1.490	0.490	0.991
318	0.004	0.306	0.003	0.203	...	0.179	0.360	0.219	0.118	0.122	0.131	0.138	0.095
322 ^c	0.250	23.050	2.280	0.550	0.080	-2.470	5.610	9.260	2.000	4.480	3.320	1.850	2.586
322	0.014	0.674	0.009	0.403	0.011	0.321	0.572	0.284	0.137	0.163	0.158	0.165	0.114

TABLE B8
RESULTS FROM THE TEMPLATE FITTING

ID	z	Member ^a	$\log \sigma$	$\log \sigma_{\text{corr}}^{\text{b}}$	$\sigma_{\log \sigma}$	Template fractions		
						B8V	G1V	K0III
1	0.2823	1	2.291	2.309	0.016	0.00	0.68	0.32
22	0.2816	1	2.290	2.308	0.020	0.00	0.89	0.11
44	0.4996	0	2.048	2.072	0.073	0.00	0.00	1.00
88	0.2846	1	1.879	1.897	0.116	0.41	0.59	0.00
116	0.2730	1	1.939	1.957	0.075	0.34	0.12	0.53
128	0.2808	1	2.210	2.228	0.023	0.00	0.66	0.34
173	0.2991	0	2.120	2.139	0.077	0.00	0.78	0.22
205	0.2736	1	2.156	2.173	0.021	0.00	0.60	0.40
241	0.2659	0	1.797	1.814	0.055	0.44	0.46	0.10
318	0.2823	1	2.112	2.130	0.030	0.49	0.44	0.07
322	0.2825	1	1.967	1.985	0.025	0.00	0.67	0.33
379	0.2857	1	2.238	2.256	0.017	0.00	0.49	0.51
412	0.2797	1	2.238	2.256	0.019	0.00	0.52	0.48
442	0.2786	1	1.795	1.813	0.166	0.00	1.00	0.00
450	0.0696	0	2.078	2.077	0.055	0.47	0.53	0.00
451	0.3853	0	2.225	2.246	0.016	0.00	0.53	0.47
479	0.2750	1	2.154	2.171	0.023	0.00	0.53	0.47
490	0.0000	0
537	0.2784	1	2.140	2.157	0.026	0.00	0.90	0.10
614	0.2727	1	2.126	2.144	0.019	0.00	0.67	0.33
637	0.2782	1	1.957	1.975	0.037	0.00	0.50	0.50
671	0.2839	1	2.344	2.362	0.018	0.00	0.34	0.66
760	0.2800	1	2.169	2.187	0.020	0.00	0.67	0.33
777	0.2823	1	2.317	2.335	0.023	0.00	0.62	0.38
844	0.2712	1	2.157	2.175	0.020	0.00	0.80	0.20
900	0.2886	1	1.961	1.979	0.052	0.54	0.46	0.00
911	0.2775	1	1.740	1.758	0.215	0.00	0.73	0.27
971	0.6151	0	2.502	2.527	0.067	0.72	0.28	0.00
1012	0.2762	1	1.931	1.949	0.037	0.00	0.83	0.17
1029	0.2834	1	1.806	1.824	0.035	0.00	0.53	0.47
1043	0.2715	1	2.037	2.055	0.025	0.00	0.50	0.50
1076	0.4036	0	1.910	1.932	0.055	0.00	0.83	0.17
1099	0.2895	1	2.117	2.135	0.153	0.47	0.36	0.18
1154	0.3869	0	2.149	2.170	0.058	0.56	0.41	0.03
1179	0.2825	1	1.803	1.821	0.068	0.10	0.37	0.52
1205	0.2706	1	1.861	1.879	0.042	0.00	0.65	0.35
1207	0.2767	1	2.092	2.110	0.035	0.00	0.24	0.76
1242	0.6155	0	2.510	2.534	0.057	0.50	0.50	0.00
1325	0.3875	0	2.280	2.302	0.042	0.00	0.66	0.34
1412	0.2728	1	1.973	1.991	0.043	0.00	1.00	0.00
1416	0.2864	1	2.004	2.022	0.103	0.00	0.00	1.00
1461	0.1896	0	2.622	2.635	0.085	0.24	0.76	0.00
1472	0.6879	0	2.478	2.504	0.076	0.00	0.66	0.34

NOTE. — ^a 1 – Galaxy is a member of RXJ0142.0+2131, 0 – spectroscopic target is not a member of RXJ0142.0+2131.

^b Velocity dispersion corrected to a standard-sized aperture equivalent to a circular aperture with a diameter of 3''4 at the distance of the Coma cluster.

TABLE B9 — *Continued*

ID	CN3883	CaHK	D4000	H δ_{A}	CN ₂	G4300	H γ_{A}	C4668	H β_{G}	Mgb	Fe5270	Fe5335	$\langle \text{Fe} \rangle$
379	0.270	23.260	2.320	-0.940	0.090	5.030	-5.020	7.380	1.990	4.610	3.190	2.800	2.998
379	0.006	0.305	0.004	0.176	0.005	0.135	0.264	0.132	0.063	0.077	0.075	0.075	0.053
412	0.290	22.510	2.260	-1.540	0.140	6.290	-6.330	7.800	1.590	4.900	2.870	2.440	2.651
412	0.006	0.269	0.004	0.164	0.005	0.123	0.244	0.130	0.060	0.076	0.075	0.075	0.053
442	0.250	17.760	2.670	-0.750	0.030	9.040	-10.190	3.840	2.500	2.420	1.250	2.190	1.721
442	0.037	1.851	0.024	0.908	0.025	0.591	1.389	0.684	0.297	0.389	0.367	0.384	0.266
450 ^b	1.280	-2.350	3.270	2.090	1.260	1.673
450	0.219	0.110	0.115	0.128	0.128	0.091
451	0.230	24.620	2.280	-0.560	0.070	5.230	-5.050	9.460	2.260	4.250
451	0.007	0.372	0.005	0.212	0.006	0.170	0.193	0.172	0.079	0.104
479	0.300	21.140	2.190	-1.290	0.130	4.990	-4.470	6.510	1.710	5.100	2.500	2.940	2.719
479	0.006	0.315	0.004	0.189	0.006	0.143	0.169	0.156	0.071	0.091	0.091	0.084	0.062
537	-1.460	0.100	5.370	-4.460	2.300	1.750	4.140	2.590	2.280	2.437
537	0.373	0.011	0.285	0.586	0.296	0.130	0.155	0.151	0.152	0.107
614	0.250	25.110	2.390	-2.130	0.110	5.040	-3.800	5.660	2.190	4.640	2.520	2.700	2.610
614	0.008	0.383	0.005	0.220	0.006	0.165	0.194	0.165	0.070	0.093	0.089	0.082	0.061
637	0.290	20.990	2.130	-1.560	0.110	5.810	-5.100	6.360	1.700	4.490	2.430	2.430	2.432

TABLE B9 — *Continued*

ID	CN3883	CaHK	D4000	H δ_A	CN ₂	G4300	H γ_A	C4668	H β_G	Mgb	Fe5270	Fe5335	$\langle\text{Fe}\rangle$
637	0.010	0.507	0.007	0.294	0.008	0.222	0.404	0.220	0.097	0.125	0.122	0.119	0.085
671 ^c	0.290	22.810	2.520	-1.330	0.130	5.860	-4.240	8.480	1.810	4.660	2.990	2.460	2.724
671	0.004	0.177	0.003	0.104	0.003	0.077	0.132	0.083	0.040	0.047	0.047	0.047	0.034
760	0.180	24.710	2.680	-2.060	0.110	8.150	-5.460	8.480	2.070	5.100	3.270	1.950	2.609
760	0.016	0.704	0.011	0.379	0.011	0.284	0.621	0.264	0.119	0.150	0.142	0.143	0.101
777	0.210	20.860	2.310	-1.930	0.130	6.600	-6.110	8.580	3.050	5.180	3.850	2.010	2.931
777	0.009	0.452	0.006	0.245	0.008	0.184	0.372	0.171	0.076	0.094	0.089	0.094	0.065
844	...	23.290	...	-1.240	0.110	4.790	-4.700	6.130	2.310	3.930	2.640	2.820	2.730
844	...	0.380	...	0.225	0.006	0.166	0.195	0.183	0.076	0.098	0.094	0.089	0.065
900 ^b	4.400	...	0.650	2.180	-1.340	-2.200	2.580	2.160	3.500	2.829
900	0.484	...	0.474	1.004	0.635	0.315	0.353	0.365	0.399	0.270
911	0.680	24.200	4.730	-1.800	...	5.030	-3.810	2.490	1.820	4.370	2.260	2.130	2.195
911	0.039	0.888	0.021	0.438	...	0.310	0.388	0.358	0.159	0.177	0.177	0.184	0.128
971	...	6.100	1.240	-0.030	0.040	2.100	-6.620
971	...	0.353	0.003	0.215	0.006	0.199	0.228
1012	0.410	26.400	2.740	-0.770	0.050	4.020	-2.420	-0.030	2.450	3.870	2.940	2.620	2.777
1012	0.014	0.541	0.008	0.282	0.008	0.256	0.288	0.287	0.117	0.137	0.132	0.126	0.091
1029 ^a	0.120	22.070	1.730	-1.380	0.120	5.840	-5.330	4.030	2.110	3.440	2.930	...	2.691
1029	0.008	0.532	0.006	0.312	0.009	0.233	0.493	0.225	0.105	0.121	0.118	...	0.108
1043	0.250	22.120	2.050	-0.420	0.110	4.870	-4.170	7.040	2.410	4.600	3.070	2.680	2.876
1043	0.006	0.320	0.004	0.203	0.006	0.152	0.175	0.158	0.069	0.087	0.086	0.082	0.059
1076 ^{a,b}	0.200	16.770	2.250	-2.390	0.120	1.370	-0.370	-2.710	0.370	3.780	3.200	...	2.939
1076	0.021	1.709	0.016	0.668	0.019	0.518	0.543	0.606	0.306	0.451	0.416	...	0.383
1099 ^b	0.180	11.350	1.470	4.460	...	2.760	-3.510	7.540	-9.030	9.470	2.810	3.200	3.007
1099	0.028	1.676	0.017	1.008	...	1.028	2.362	1.318	0.764	0.860	1.137	1.276	0.854
1154 ^b	...	7.210	1.520	3.000	...	0.920	0.840	1.970
1154	...	0.382	0.004	0.226	...	0.217	0.234	0.268
1179 ^{b,c}	0.140	13.760	1.800	-1.110	...	4.360	-8.570	5.200	-3.730	3.580	2.720	1.920	2.324
1179	0.016	0.974	0.011	0.550	...	0.538	1.176	0.625	0.308	0.273	0.274	0.290	0.200
1205	0.160	23.220	2.080	-1.380	0.150	5.260	-4.270	9.080	2.720	4.050
1205	0.011	0.573	0.007	0.335	0.009	0.230	0.270	0.243	0.098	0.123
1207	0.250	26.120	2.530	-0.810	0.100	5.910	-7.060	5.810	1.230	1.840	2.670	2.300	2.486
1207	0.011	0.480	0.007	0.275	0.008	0.212	0.261	0.227	0.100	0.129	0.119	0.116	0.083
1242	0.080	10.100	1.600	5.370	...	9.000	-0.800
1242	0.012	0.819	0.008	0.441	...	0.427	0.433
1325 ^b	0.160	20.270	2.100	-1.700	0.130	4.910	-2.030	8.770	2.420
1325	0.005	0.295	0.004	0.166	0.005	0.130	0.144	0.132	0.060
1412 ^c	...	21.970	...	-1.020	0.100	4.970	-2.180	4.510	2.750	3.700	2.620	3.890	3.253
1412	...	0.434	...	0.288	0.008	0.200	0.237	0.227	0.096	0.125	0.116	0.106	0.079
1416 ^b	0.310	33.550	2.660	3.050	...	3.380	-0.140	9.430	-0.780	3.620	-1.220	2.850	0.818
1416	0.023	1.021	0.014	0.518	...	0.346	0.751	0.363	0.174	0.186	0.186	0.192	0.134
1461 ^b	2.590	-1.470	4.360	-7.770	-1.790	1.700	3.110	2.406
1461	0.262	0.288	0.503	0.161	0.209	0.232	0.284	0.183
1472	0.120	16.390	1.600	6.540	0.050	4.640	-2.820
1472	0.005	0.320	0.004	0.220	0.006	0.245	0.273

NOTE. — For each object, the first line gives the value of the line index and the second line denotes the uncertainties.

^a $\langle\text{Fe}\rangle$ is calculated from Fe5270 only assuming the best fitting linear relation between Fe5270 and Fe5335 derived from cluster members.

^b Emission-line galaxy. ^c H δ_A + H γ_A is derived from H δ_A only assuming the best fitting linear relation between H δ_A and H δ_A + H γ_A for cluster members.

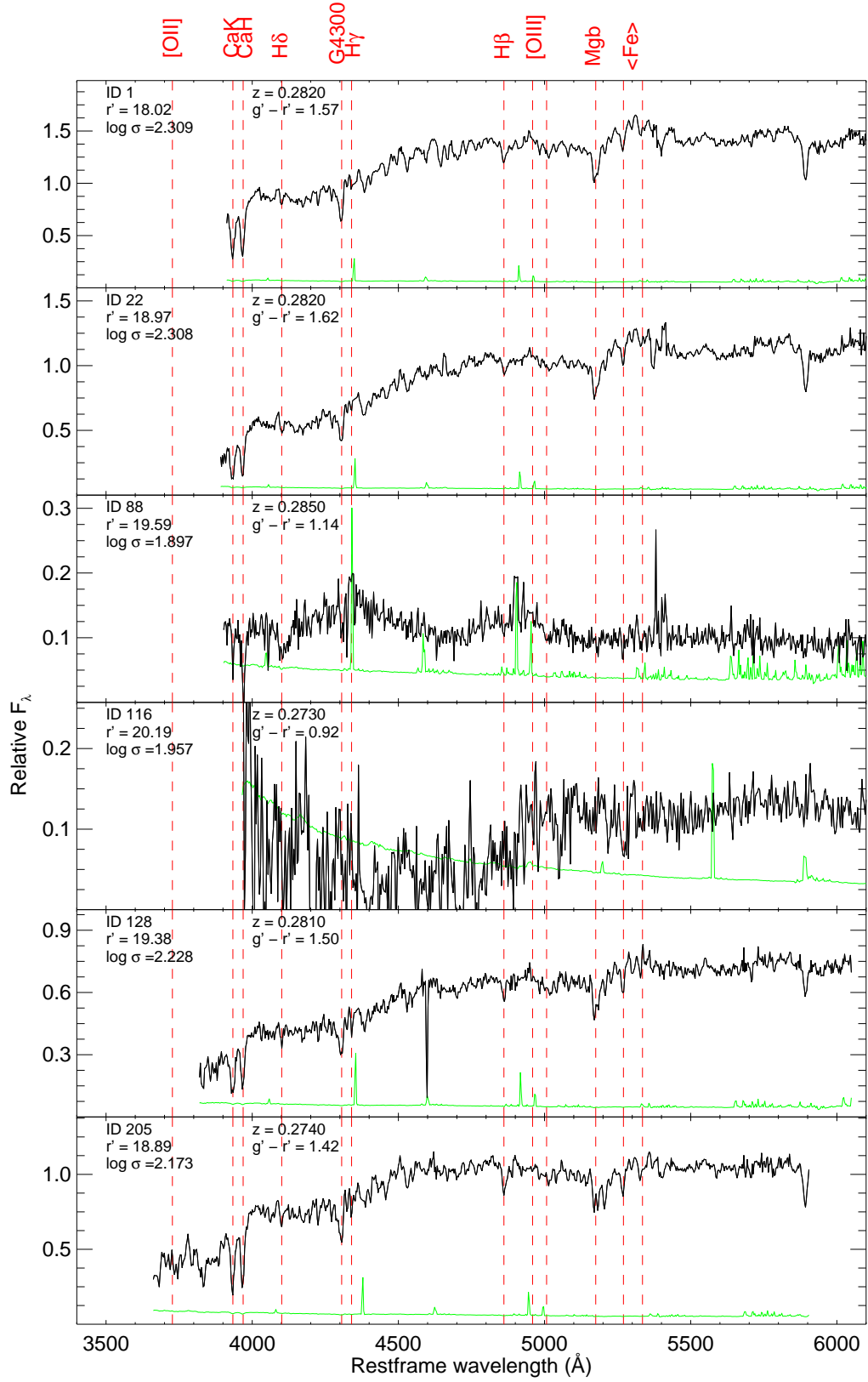


FIG. B10.— Extracted 1D spectra of cluster members in the rest frame. The black line represents the flux-calibrated spectrum, the green line is noise multiplied by a factor of two for clarity. The positions of the most prominent spectral features are labeled with vertical dashed lines.

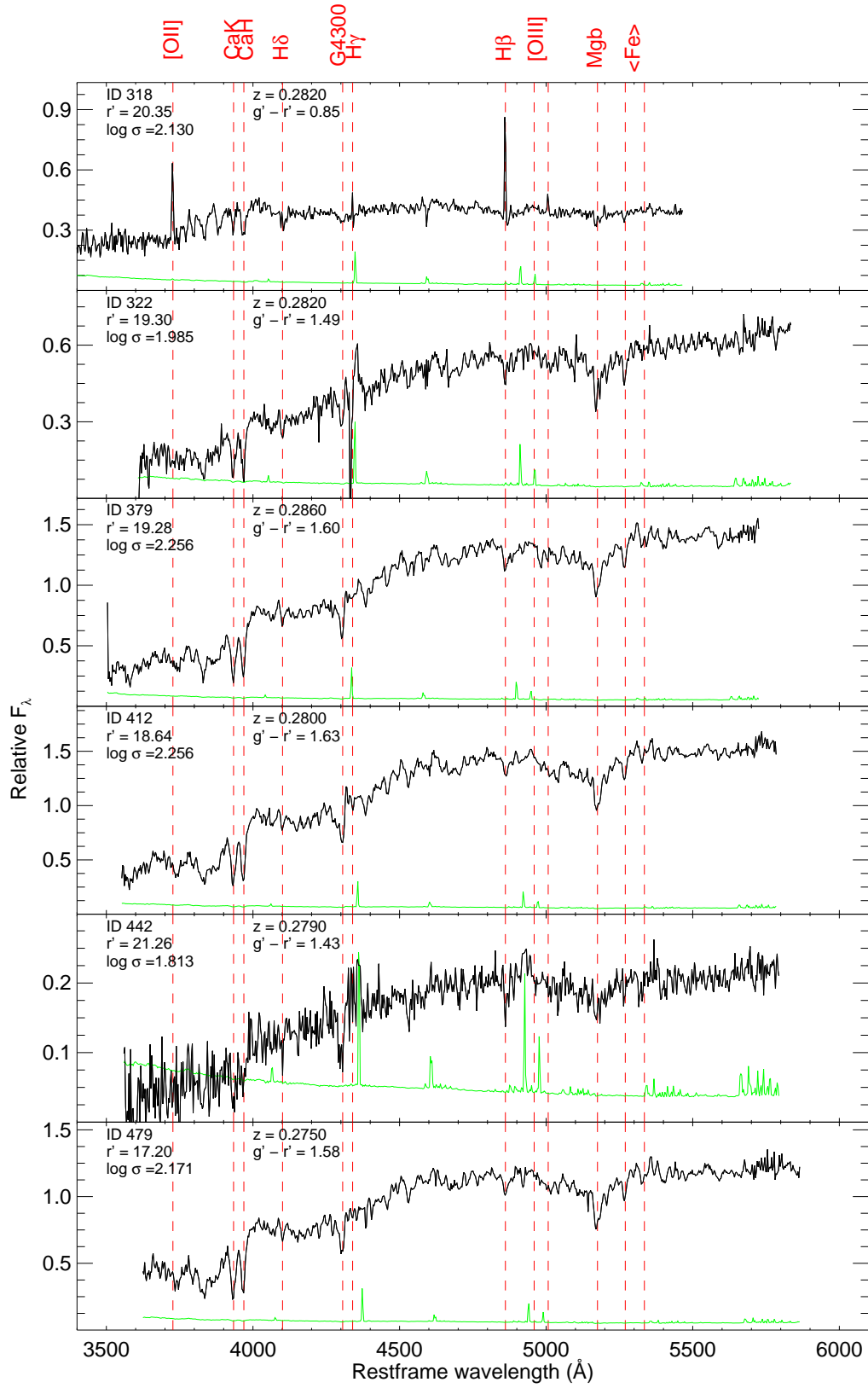


FIG. B10.— Continued.

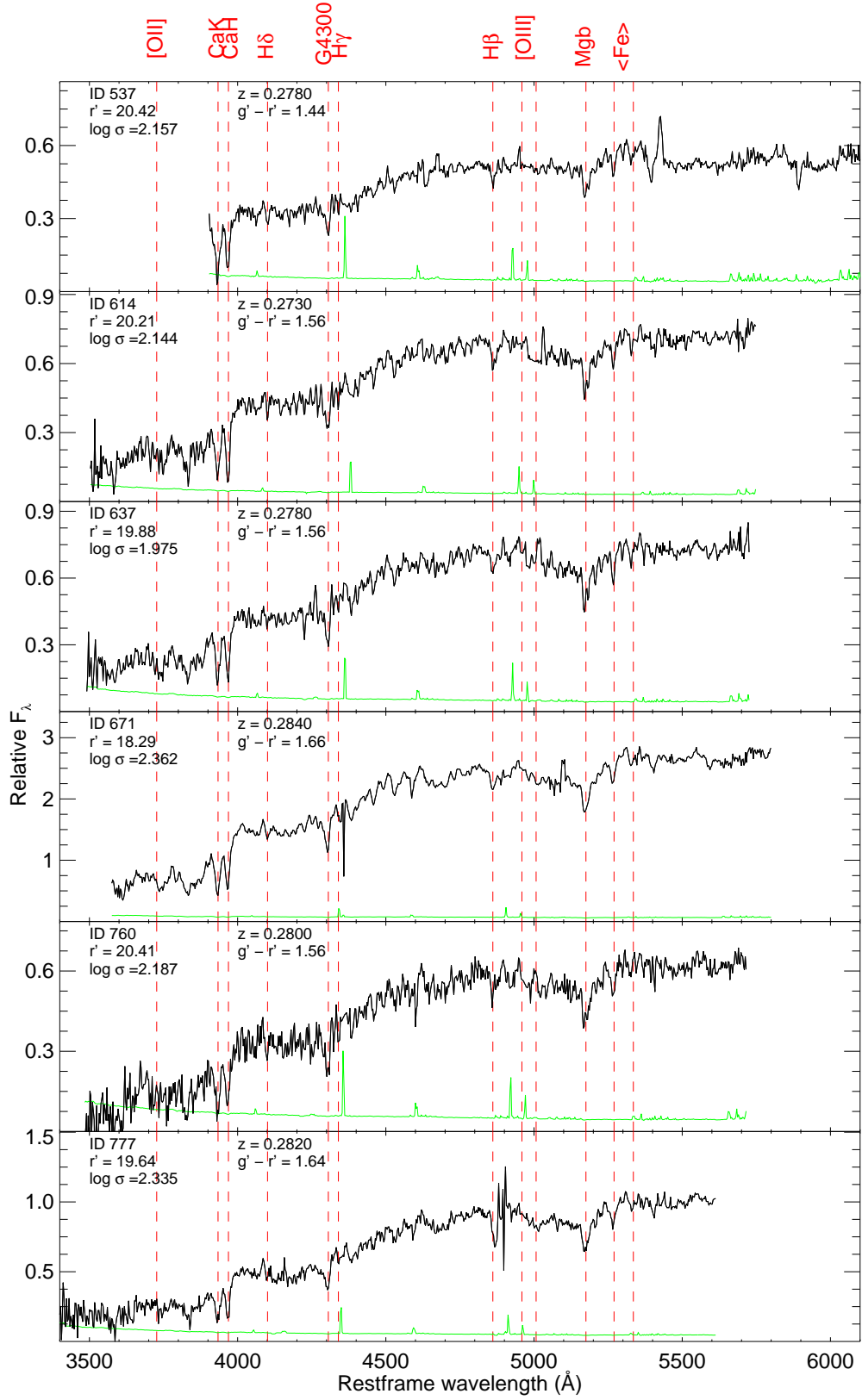


FIG. B10.— Continued.

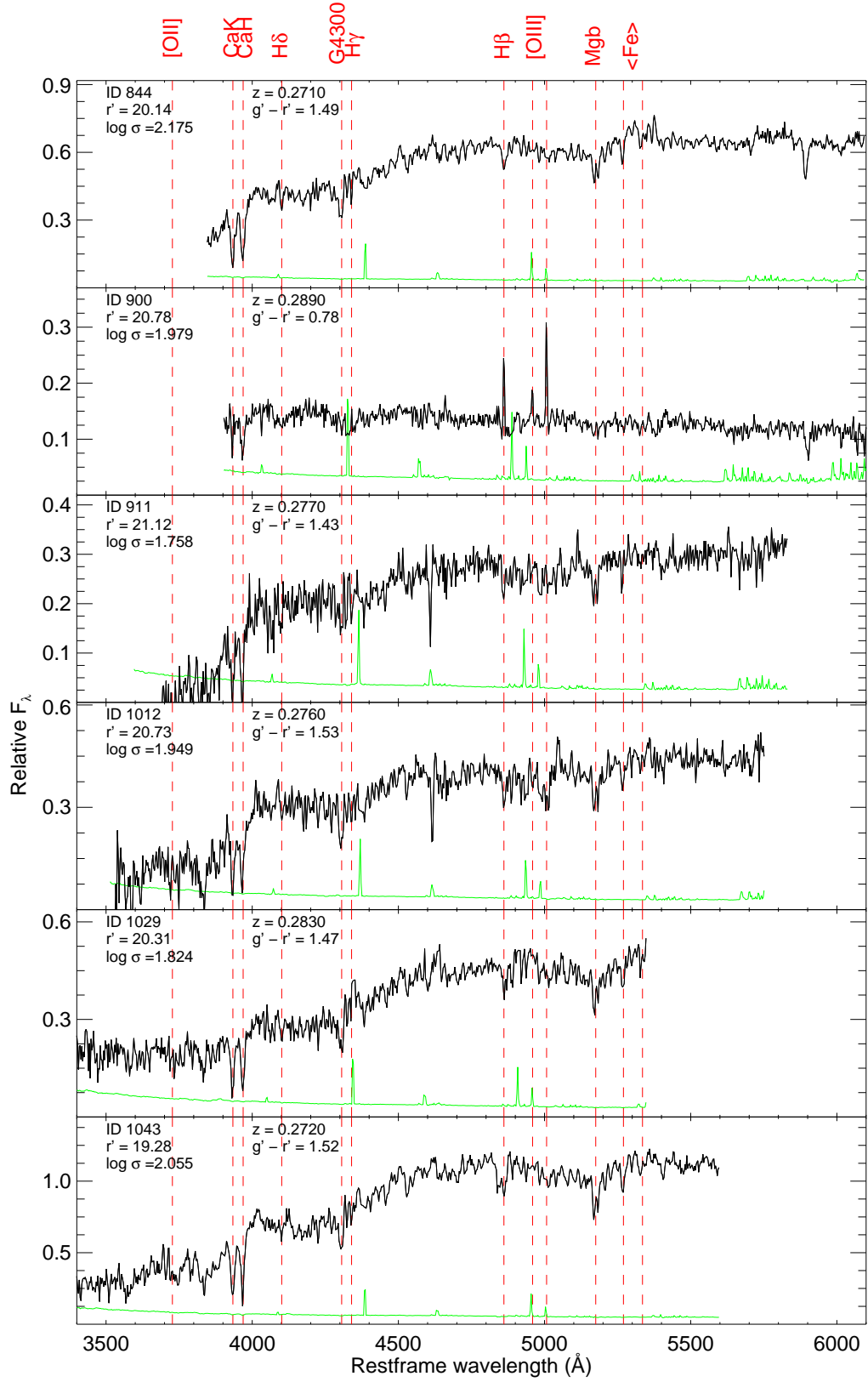


FIG. B10.— Continued.

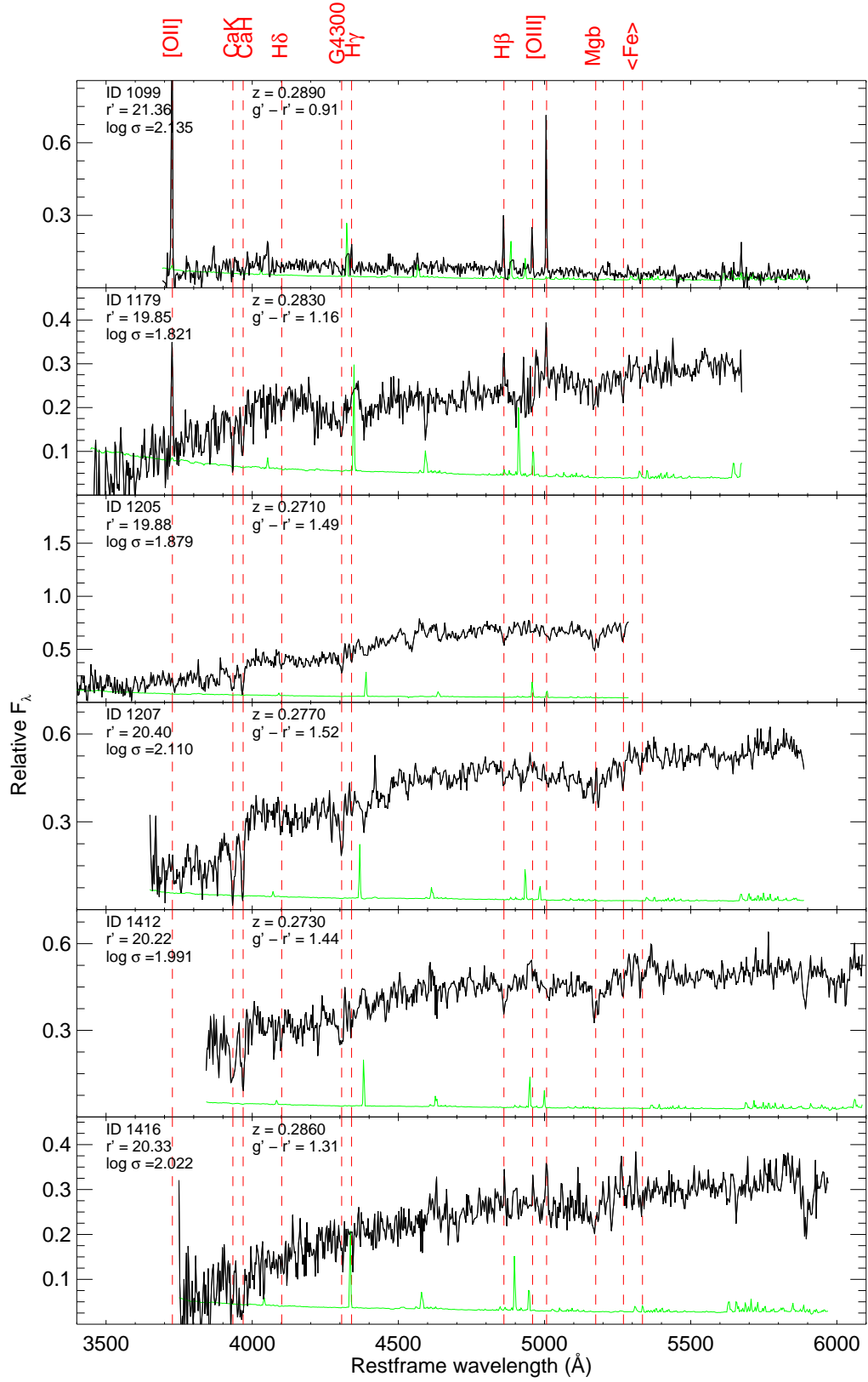


FIG. B10.— Continued.

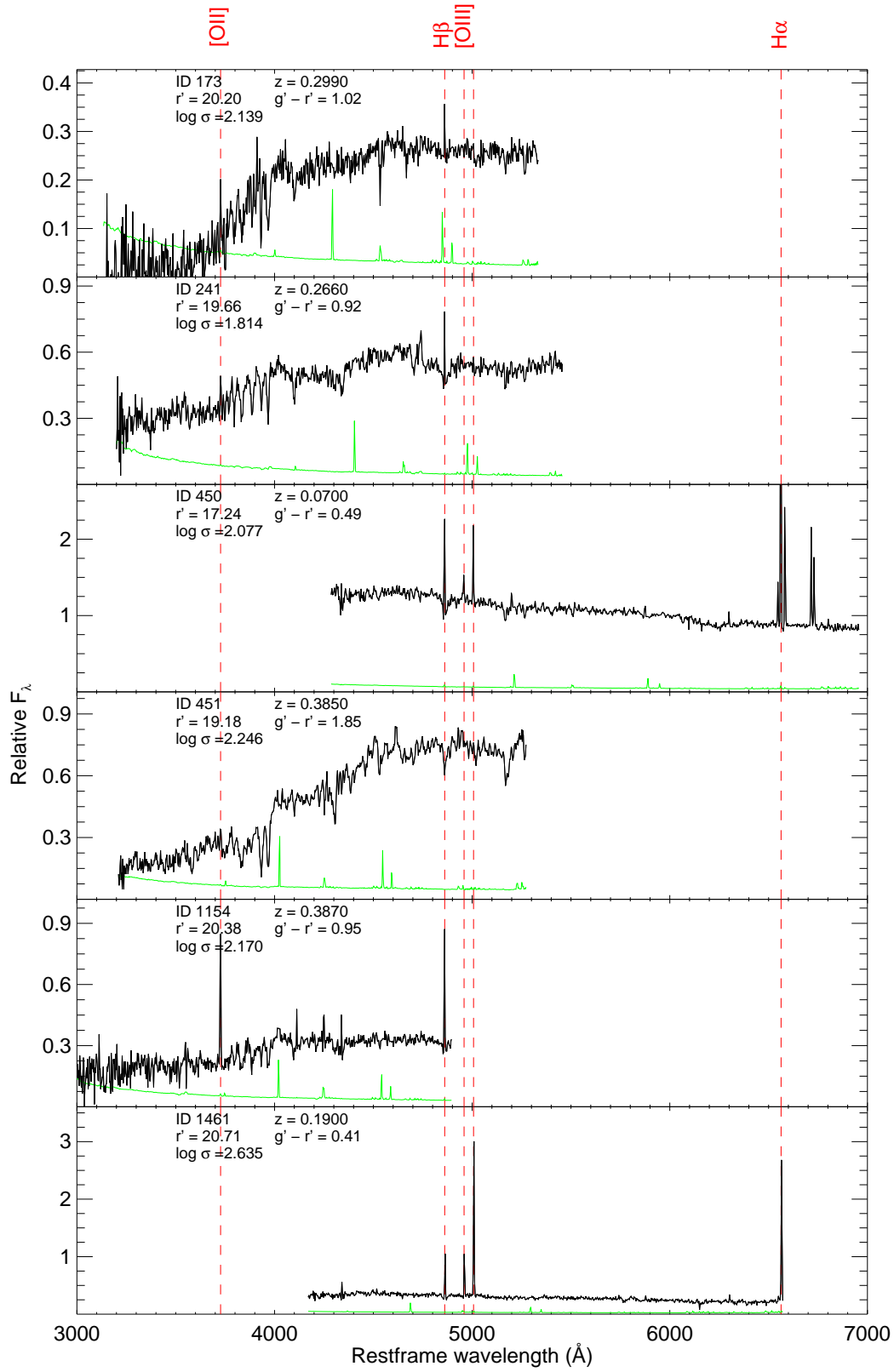


FIG. B11.— Extracted 1D spectra of non-members in the rest frame. The black line represents the flux-calibrated spectrum, the green line is noise multiplied by a factor of two for clarity. The positions of the most prominent emission lines are labeled with vertical dashed lines.

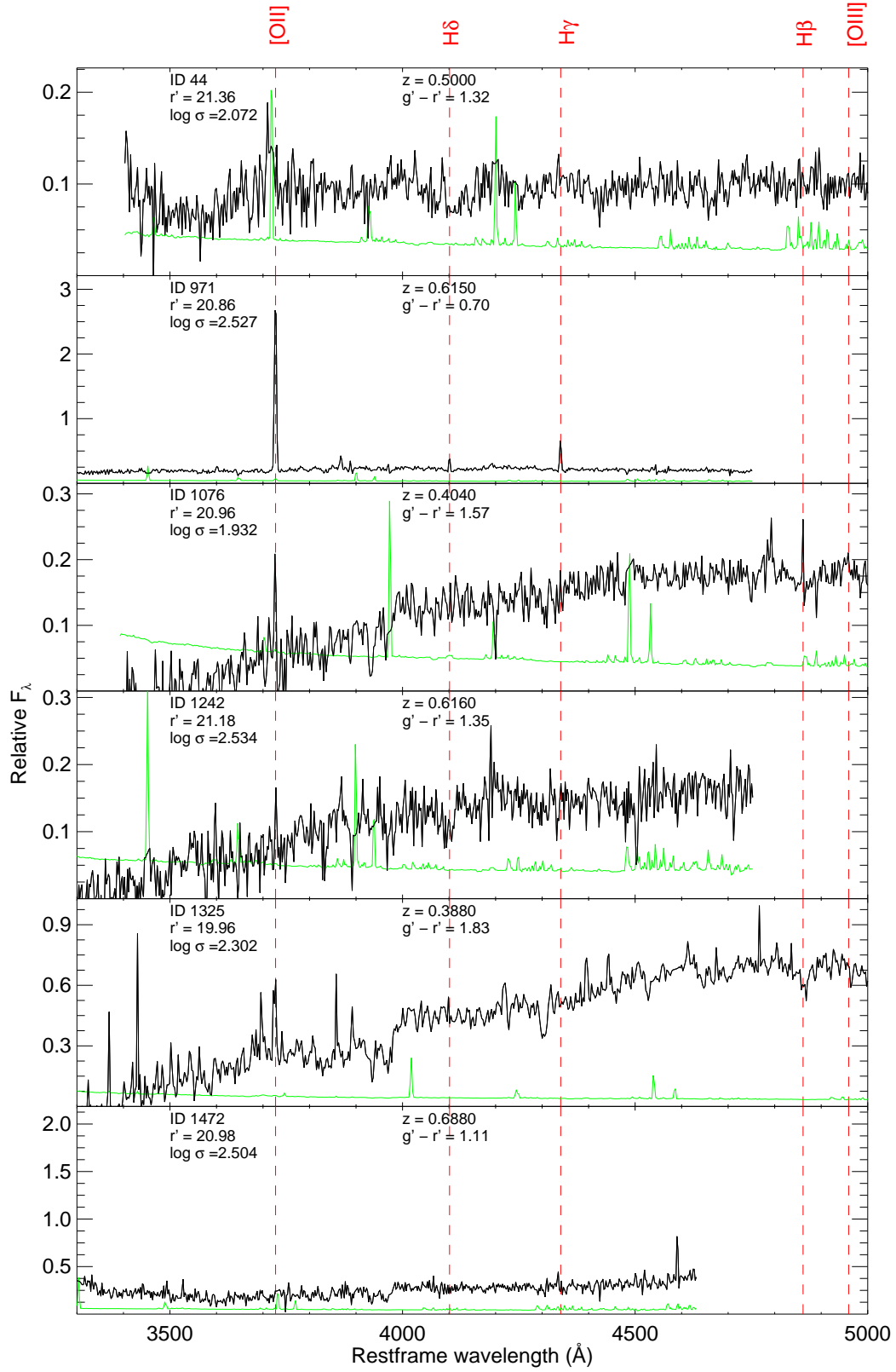


FIG. B11.— Continued.

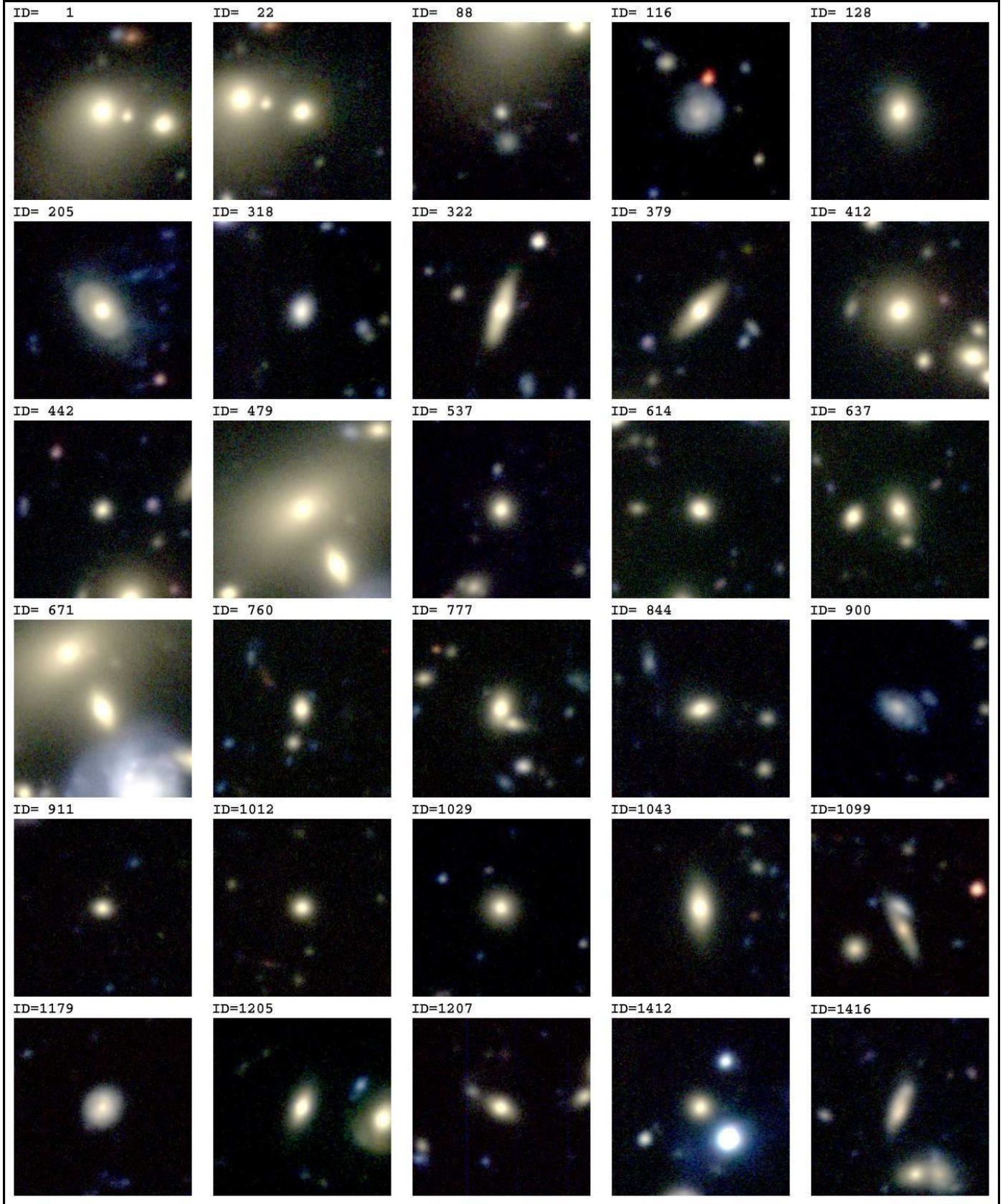


FIG. B12.— Postage stamps of cluster members in RXJ0142.0+2131. Each frame is $17''.5$ by $17''.5$, corresponding to $75\text{kpc} \times 75\text{kpc}$ at $z = 0.28$, with the spectroscopic galaxy at the centre. North is up, East is left. The stamps are produced from the GMOS-N g' , r' , i' images. The galaxy ID is indicated at the top left of each stamp.

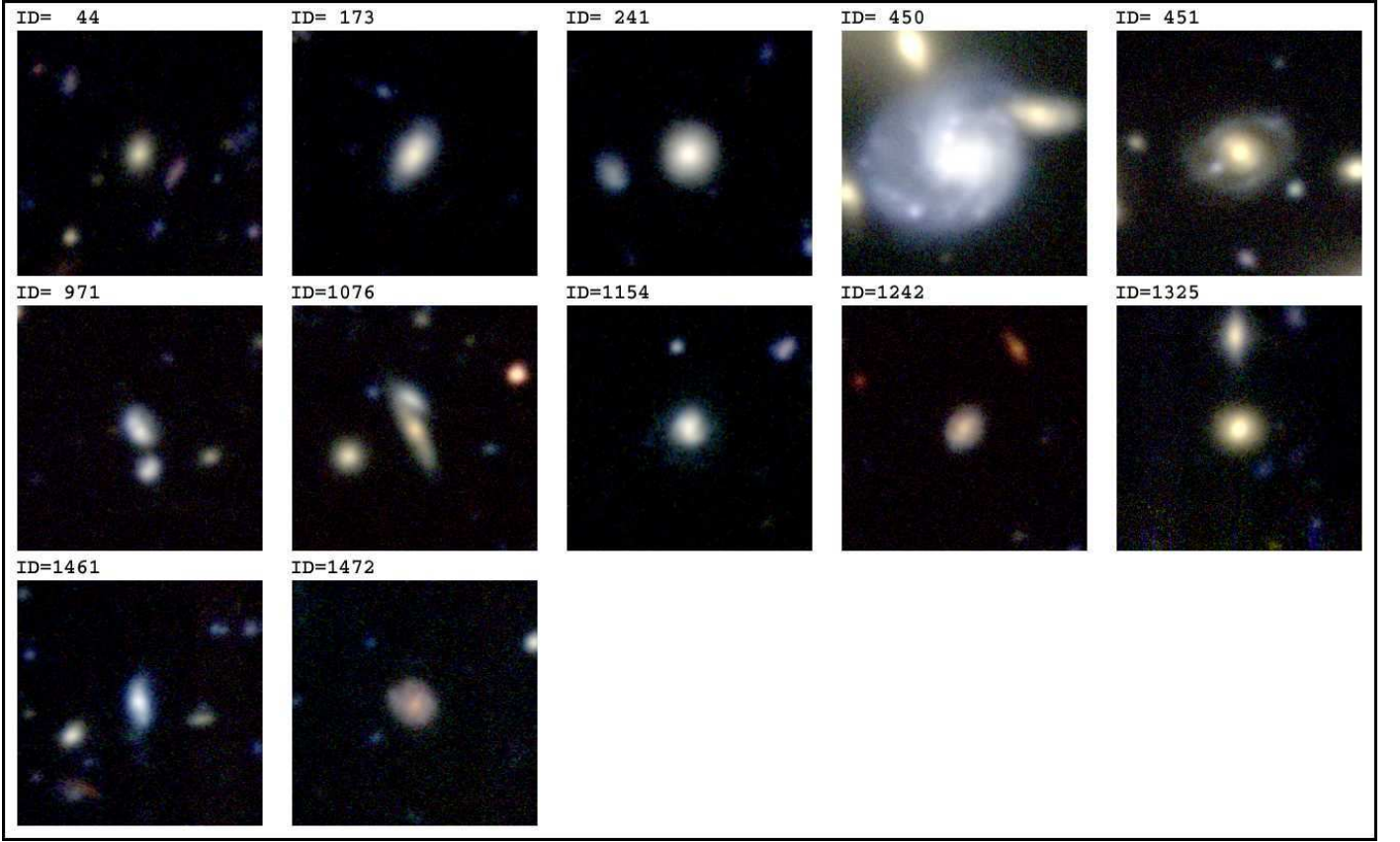


FIG. B13.— Color images of the non-cluster members in the spectroscopic sample. The images are equivalent to those in Figure B12.